ELSEVIER

Nuclear Engineering and Design 189 (1999) 7–57

Nuclear Engineering and Design

Lower head integrity under steam explosion loads

T.G. Theofanous [a,*], W.W. Yuen [a], S. Angelini [a], J.J. Sienicki [b], K. Freeman [a], X. Chen [a], T. Salmassi [a]

[a] *Center for Risk Studies and Safety, University of California, Santa Barbara, CA 93106, USA*
[b] *Reactor Engineering, Building 208, Argonne National Laboratory, 9700 South Cass Avenue, Argonne, IL 60439, USA*

Received 24 August 1998; accepted 24 November 1998

Abstract

Lower head integrity under steam explosion loads in an AP600-like reactor design is considered. The assessment is the second part of an evaluation of the in-vessel retention idea as a severe accident management concept, the first part (DOE/ID-10460) dealing with thermal loads. The assessment is conducted in terms of the risk oriented accident analysis methodology (ROAAM), and includes the comprehensive evaluation of all relevant severe accident scenarios, melt conditions and timing of release from the core region, fully three-dimensional mixing and explosion wave dynamics, and lower head fragility under local, dynamic loading. All of these factors are brought together in a ROAAM probabilistic framework to evaluate failure likelihood. The conclusion is that failure is 'physically unreasonable'. © 1999 Elsevier Science S.A. All rights reserved.

Keywords: Steam explosions; Reactor safety; In-vessel retention; Severe accident management

1. Introduction

This paper constitutes the second and final part of a comprehensive assessment of the 'in-vessel retention' idea as a severe accident management concept. The first part (Theofanous et al., 1995a) dealt with the thermal loading aspects of the problem. This second part addresses structural integrity under steam explosion loads potentially triggered in the lower plenum during the early melt relocation process from the core region. As was the case in the first part, this second part has been put together with two purposes in mind: first, to demonstrate the effectiveness of the concept for an AP600-like design; and second, to provide a readily adaptable path for its consideration in other designs.

The accident management strategy is to flood the reactor cavity, submerging the reactor vessel. The concept is based on the idea that the lower head, cooled externally, will be able to arrest the downward relocation of a degraded (melting) core. Although the thermal aspects of lower head integrity under such conditions have been studied extensively, this is the first work on structural integrity under steam explosion loads.

* Corresponding author. Tel.: +1-805-893-4900; fax: +1-805-893-4927.
E-mail address: theo@theo.ucsb.edu (T.G. Theofanous)

PII: S0029-5493(99)00028-X

The status of existing knowledge, incidental in considering steam-explosion-induced containment failure in pressurized water reactors (PWRs) (the so-called α-mode failure), can be summarized simply as follows.

- Bohl and Butler (1985) used a simple single-degree-of-freedom spring-mass model of the reactor vessel lower head in a SIMMER-II model of a steam explosion process. Failure occurred at 2.7 ms, and the explosion yield of 1460 MJ was found to partition about evenly in the upward and downward directions—850 MJ were delivered to an upward accelerated slug, while 610 MJ were vented downward.
- Theofanous et al. (1987), as part of a comprehensive α-mode failure study, loaded a finite element model (using the STRAW computer code) with a simple, thermodynamics-based equation of state of the explosion zone in the lower head. Eleven calculations were carried out for a variety of explosion characteristics (parameterized by volume of the explosion zone and the fuel and steam volume fractions in it), spanning the range of energy yields from 0.4 to 11.6 GJ. They found that explosions with yields above ~ 1 GJ produced lower head failure. Fuel masses involved were from a few to some tens of tons, pressures were in the kilobar range, and failures occurred at ~ 1 to 2 ms.
- Turland et al. (1995), in their α-mode failure assessment for Sizewell, decided against taking credit for explosion venting due to lower head failure. They noted that the lower head static capability in Sizewell is ~ 650 bar, that there is no evidence of the kilobar pressures found from ideal thermodynamic models, and that experiments and more realistic modeling suggest that for 1 GJ explosions, peak pressures will more probably be in the range 400–800 bar.

Both Theofanous et al. (1987) and Turland et al. (1995) had indicated the need to re-examine these results, once the capability to properly represent the dynamic explosion loads became available. This time has come.

This paper consists of four main technical sections. There are also a number of supporting appendices, which can be found in DOE/ID-10541. Section 3 addresses structural failure criteria, Section 4 deals with the melt relocation characteristics, and the following two sections present the quantification of steam explosion loads. The integration of this material toward assessing the likelihood of lower head failure is presented in Section 7. The aim of these sections, their inter-relation, and some overall perspectives helpful in understanding the nature of the main technical issues are provided in Section 2. Section 8 is devoted to the consideration of late water addition, on top of a fully molten pool, contained in the lower head. The paper comes to an end with conclusions and recommendations, presented in Section 9.

Further to the appendices already noted, this paper is technically supported by two verification reports, one each for the two main analytical tools utilized, the ESPROSE.m (Theofanous and Yuen, 1998a) and PM-ALPHA (Theofanous and Yuen, 1998b). These are important companion documents to the present work. It may be helpful for the reader to consult also 'The Study of Steam Explosions in Nuclear Systems' (Theofanous et al., 1995b); it has been written as a 'primer' on the steam explosion problem, and includes a description of our general approach. Finally, it may be handy to have the first part of this 'in-vessel retention' work, the one concerned with the 'thermal aspects,' as mentioned already. The two parts are connected not only in regards to the relocation phenomenology, but they also employ a similar treatment for estimating thermal loads from a molten pool—to the lower head in one case and the core reflector in the other. Taking these connections into account, the exposition here avoids duplication to the extent possible. For purposes of convenience, DOE/ID-10489 (Theofanous et al., 1995b) and DOE/ID-10460 (Theofanous et al., 1995a) will be referred to as 'The Study' and the 'IVR Report', respectively.

Further background on the subject of steam explosions can be found in the proceedings of a CSNI Specialists' Meeting in Santa Barbara (CSNI, 1993), of two joint US–Japan seminars (OJI, 1993; AMIGO Seminar, 1995), and of the Second Steam Explosion Review Group (SERG2,

1995). A review article is also available (Fletcher and Theofanous, 1997).

2. Problem definition and overall approach

The lower head of the AP600 can take a static load of up to ~500 bar, and for impulses of millisecond duration, it would not be expected to yield well into the kilobar range (see Section 3). Until rather recently, empirical evidence indicated that such pressures are unrealistically high, even for large-scale steam explosions, and on this basis, the Sizewell assessment, as already noted, did not take credit for venting due to lower head failure. At this time, we have experiments, albeit constrained to one dimension (Hohmann et al., 1995), and calculations (Theofanous and Yuen, 1994), that have produced pressures in the kilobar range, and lower head failure cannot be dismissed as readily any longer.

The experiments involved aluminum oxide melts (~2800°C) in kilogram quantities, mixed with water along the length of a 1-m-long tube (the KROTOS facility). The calculations were carried out with the 'microinteractions' model (Yuen et al., 1994; Yuen and Theofanous, 1995), which for the first time allowed for fragmentation-and-mixing constitutive laws appropriate for propagation. This model provided consistent interpretations of these aluminum oxide tests (as well as of previous tests with molten tin that fizzled), and more generally demonstrated the possibility of supercritical detonations even with lean (in melt) premixtures (Fletcher and Theofanous, 1997). This model then led to the ESPROSE.m code. It, together with the PM-ALPHA code needed for premixing, forms the essential basis for the present work.

On balance, the calculations also demonstrated that peak pressures decay quickly with distance (away from the explosion zone in two-dimensional geometries) and with time, and also through venting at free interfaces, such as the coolant pool surface (Theofanous and Yuen, 1994) or a weak structural boundary. Unfortunately for the present problem, the explosion can occur in the immediate vicinity of the lower head, and upward venting is relatively constrained by the presence of the core support plate (resting upon the core support structures—see IVR Report), carrying, in addition to the core barrel and reflector, essentially the whole reactor core on it. Thus, it is not clear how to apply the mentioned mitigating factors, which in this case may even be of marginal value. Clearly, calculations taking into account all the key three-dimensional (3D) features of the geometry are necessary, and the 2D PM-ALPHA and ESPROSE.m codes were extended to 3D especially for this purpose (see Sections 5 and 6).

Also, it is important to note that within the limited experience with reactor fuel materials (UO_2, ZrO_2) we have no evidence of explosions, but rather extensively voided premixtures (Huhtiniemi et al., 1995), nor is it known whether or under what conditions such premixtures can be triggered to explode. We are currently working to obtain, experimentally, constitutive laws for microinteractions of these materials, but until definitive evidence points otherwise, we will assume, conservatively, that spontaneously triggered explosions in reactor geometries cannot be excluded.

Before we get into the specifics, another interesting general perspective on the potential for failure can be obtained from the results of Theofanous et al. (1987). Based on an isochoric, and instantaneous equilibration (between the fuel and mixed coolant), followed by an ideal thermodynamic path in the expansion, the results are conservative for our present purposes. From the explosion yields found, over a wide range of mixing zone sizes and mixture compositions, and by scaling back, we find that somewhere between 3 and 5 t of fuel must participate to produce a 1 GJ explosion, and consequently incipient lower head failure. Such quantities of 3–5 t are about one order greater than what can be reasonably found in transit within the lower plenum (see Section 4), or what can be found possible to premix accounting for water depletion (see Section 5) and its effects on propagation (see Section 6).

Our present approach is founded on the risk oriented accident analysis methodology (ROAAM), as was the case for the companion

IVR Report. A key feature of ROAAM (see Appendix A of DOE/ID-10541) is the decomposition of a complex problem into a set of 'causal relations' constrained by well-defined and tested physics, and a set of 'intangible parameters' that can only be qualitatively specified. The causal relations are quantified by best estimate physics accounting for uncertainties. The intangible parameters are specified in a conservative fashion, to bound uncertainties, and *then* quantified using a probability scale (see Table A.1 in Appendix A of DOE/ID-10541). Reconstitution of the problem is carried out according to the probabilistic framework that defines the interconnections between the various elements. Results are interpreted back in qualitative terms by employing the probability scale in reverse. An overview of how this whole procedure works out for the problem at hand is given later. The actual substance can be found in the following five sections.

The geometry is illustrated in Fig. 1. As noted in the IVR Report, and further explained in Section 4, a downward relocation path of the melting core materials through the core support structure is not physically reasonable (this term is used in the sense of Table A.1 of Appendix A of DOE/ID-10541). Also, because of the highly retentive

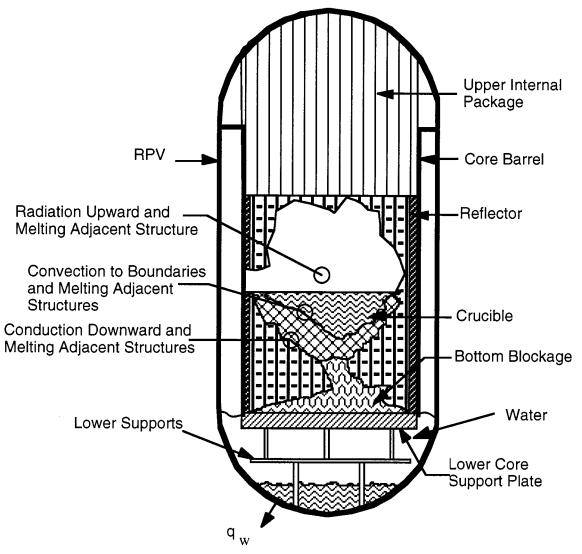

Fig. 1. The overall geometry, and early stages of core degradation.

character of the reflector (and the core barrel), and the relatively flat core power distribution, we expect that the first relocation will occur off to the side and from a fully developed melt pool. We will show in Section 4 that the melt participating in the initial relocation will have to be oxidic, and that there is not much uncertainty about its temperature (to affect the steam explosion results). The main questions are on the location and size of the failure (melt-through), and these are indeed tough questions, especially that of size. This parameter has to be approached at this time as an 'intangible'.

From the location and size of the core barrel breach, we can obtain the melt relocation rate into the downcomer, and through it into the lower plenum. The water would be saturated with the primary system completely depressurized to the containment pressure, nominally taken at 1 bar (see IVR Report, Table 7.3). In Section 5, we show that premixtures developed under these conditions would be highly voided, and that the lower head curvature, in confluence with the edge of the core support plate, creates conditions favorable for fuel accumulation and further voiding. Also, we show that deeper penetrations are confined along the wall and are accompanied by more wide spread voids within the lower plenum water, as illustrated in Fig. 2. The main unknown here is about the evolution of the melt characteristic length scale(s), both following its thermal–hydrodynamic interaction with the vessel wall, as well as during its mixing with the coolant. As explained in 'The Study', this unknown is subject to certain compensating effects that allow a reasonably robust enveloping approach; namely, that the enhanced explosive potential of an extensively broken-up melt is moderated by the much higher water depletion, and vice versa, that the higher explosivity of a premixture with reduced voiding is moderated by the reduced melt interfacial area for microinteractions. In PM-ALPHA, the degree of break-up is controlled by the assumed initial size of the melt particles, d_{fo}, and a parameter β that determines the break-up rate (the source term in the interfacial area transport equation). Both d_{fo} and β are treated as intangible parameters, with the intent to conservatively bound their ef-

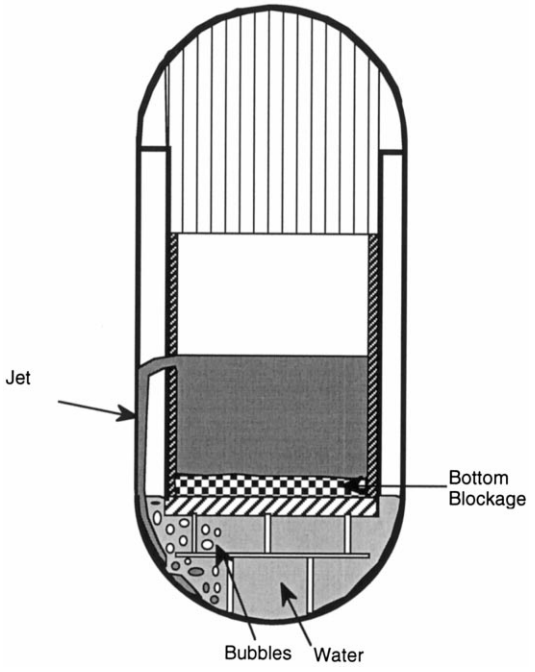

Fig. 2. Melt pour geometry, and lower plenum voiding during premixing.

fect. The end result of this step is a set of premixture map histories (3D composition distributions), each one characterized by the likelihood assigned to the respective melt release rate.

These 'characteristic' premixtures are then made to explode using the ESPROSE.m-3D code. The main question now is on the timing of the trigger, and this is again intangible (Fletcher and Theofanous, 1997). Again, there are compensating effects (see 'The Study') in that a delayed trigger implies a larger amount of fuel available to explode, and longer acoustic unloading times, but it also implies a more extensively voided lower plenum, and hence resistance to energetic propagation and/or dampening of the result if an explosion is not prevented altogether. In much deeper pools, as in some exvessel geometries, a delayed trigger implies also a significant amount of fuel freezing, and a corresponding decrease in the amount of melt available to participate in the explosion. In Section 6, we explore these trends further, and end up with an envelope of the trigger time, as an intangible, for each of the characteristic premixtures. Moreover, we come to the conclusion that, because of the extensive voiding, we need only be concerned with the first relocation event, and only for early triggers in it; i.e. basically, an 'as is' lower head structural capability. Each triggered explosion calculation yields a pressure–time history for each local element of the lower head. Through the probability of the respective premixture, each such calculation is characterized by a corresponding probability expressing the likelihood of the resultant load.

Finally, these results are used in two different ways to determine the margins to failure: first, by comparison (see Section 7) with the lower head fragility established in Section 3; second, by directly loading a finite element model and examining the strains obtained in relation to strains expected to produce failure (Section 7). Both the subject of structural failure criteria and material constitutive behavior, accounting for strain rate effects, are discussed in Section 3. The fragility is developed by applying this discussion to the results of a finite element model under various kinds of loading patterns. In particular, we show that for the class of loadings relevant here, material deformation, and failure, can be characterized by the impulse (the pressure integral over time), and the wall fractional area over which this impulse is applied, and that these results can be generalized into a convenient-for-use fragility applicable to any impulse–area combination, within the broader ranges examined. Both approaches provide very clear evidence that failure is physically unreasonable.

The process described is schematically illustrated in Fig. 3. This is the probabilistic framework for this problem. As shown, the codes provide the three causal relations, and as discussed, the 'break-up' and 'trigger time' intangibles are conservatively enveloped. Describing how this is actually achieved is the main task of Sections 5 and 6. The fragility is expressed in the form of a cumulative density function (cdf1), and its convolution with pdf3 provides a numerical measure of the total failure probability. Finally, this is converted to the proper qualitative measure of likelihood by applying in reverse the same probability scale used to quantify the intangibles.

3. Structural failure criteria

In this section, our task is to develop a methodology for assessing likelihood of lower head failure under localized, millisecond-duration pressure pulses with peaks in the kilobar range. Keeping with our basic-principles approach, we build gradually towards the final result, from a characterization and understanding of the dynamics (of material deformation, i.e. strains) due to uniformly-distributed highly transient loads, to strain rate effects on material constitutive behavior, to effects of load non-uniformity. Our basic tool is a shell element model with the computer code ABAQUS (Version 5.5, implicit numerics), but we also make use of a simple analytical solution to better ground the numerical effort. Moreover, recognizing that the time-duration of the loads of interest here is less than the structure natural frequency, we expect that peak strains would be basically independent of the details of the pressure pulse shape, and direct our effort towards generalizing the numerical results, to allow convenient characterization of the response under any pulse temporal and spatial characteristics. The final step is to translate this generalized strainloading result to a 'fragility'; i.e. to a failure probability as a function of loading. This is done by examining the strain–failure relationship, both in terms of the physics of failure, as well as available experimental data and related correlations.

Also in keeping with our basic-principles approach, we chose to simplify in several respects by taking a conservative approach. These include:

- ignoring fluid–structure interaction in the determination of the loads (i.e. in Section 6, we assume a rigid structure);

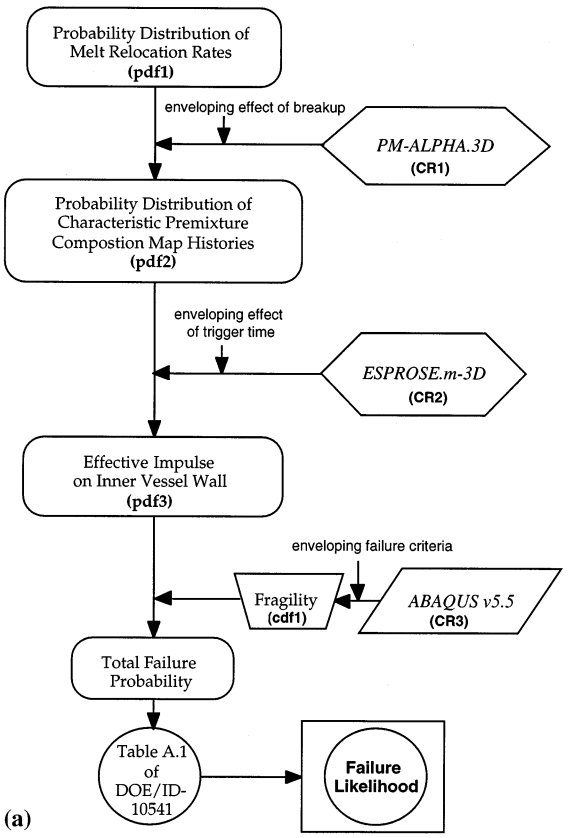

Fig. 3. (a) Schematic diagram of the probabilistic framework utilized in this work. (b) Illustration of the probabilistic framework utilized in this work.

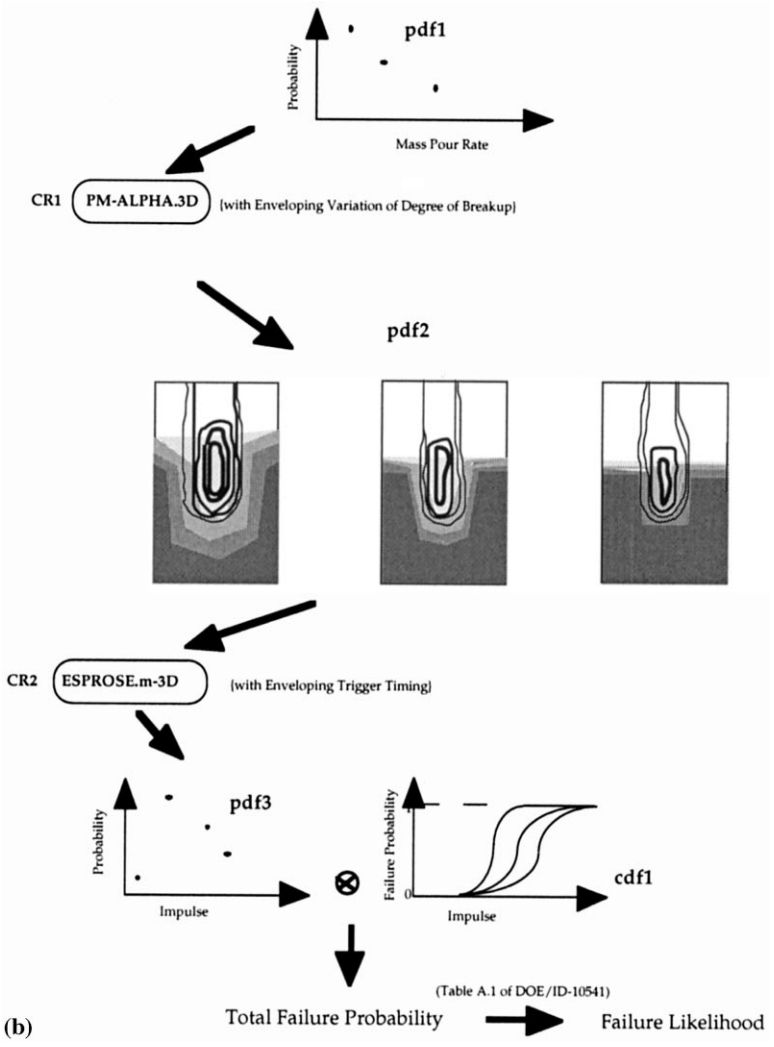

Fig. 3. (*Continued*)

- assuming elastic perfectly plastic material behavior, i.e., ignoring strain hardening effects; and
- making use of a yield stress that is somewhat lower than the ASME code for SA508 Class 3 steel (330 vs. 345 MPa), and significantly lower than the as-tested value of the material (330 vs. 450 MPa) provided to us by Japan Steel Works, which is one of the designated AP600 vessel suppliers,

These constitute additional margins that may be good to keep in mind for future applications.

3.1. Load–strain behavior

Let us begin with an analytical solution due to Duffey and Mitcheli (1973). It is based on the energetics of a sufficiently short pressure pulse, requiring that the kinetic energy of the shell wall becomes plastic strain energy of deformation. They worked out the result for a cylindrical shell, axisymmetrically loaded, and incorporated strain rate effects on the yield stress. For mild steel, this dynamic yield stress was obtained from Bodner and Symonds (1962) as

$$\sigma_y^D = \sigma_y\left[1 + \left(\frac{\dot{\varepsilon}}{D}\right)^{1/p}\right] \quad (1)$$

where σ_y is the static yield stress, $\dot{\varepsilon}$ is the strain rate, and D and p are material parameters (for mild steel equal to 40.4 s^{-1} and 5, respectively). This simple approach was shown to work quite well for thin cylindrical shells subjected to point explosives at the interior axis of symmetry, yielding an axially varying load on the interior wall. In particular, neglecting bending moments, they applied this one-dimensional (1D) formulation in terms of the local loads, and found reasonable comparisons with the observed local (axially varying) deformations.

Applying the same approach to a uniformly loaded spherical shell, we obtain, for the plastic equivalent strain (see Appendix A),

$$\varepsilon = \frac{I^2}{2\rho\delta^2\sigma_{y_o}^D} \quad (2)$$

where I is the delivered impulse (i.e. the pressure–time integral), δ is the wall thickness (15 cm here), and σ_y^D is the dynamic yield stress based on the initial strain rate, i.e.

$$\sigma_{y_o}^D = \sigma_y\left[1 + \left(\frac{\dot{\varepsilon}_o}{D}\right)^{1/p}\right]; \qquad \dot{\varepsilon} = \frac{I}{\rho\delta R} \quad (3)$$

We can thus quickly estimate that for a 10% strain, we need impulses of the order of 0.15 MPa s, and that for this condition, the strain rate effect amounts to 50% credit (i.e. 50% larger impulse). It is interesting to note that, by coincidence, the as-tested value of the yield stress is $\sim$50% larger than the value used in the computations here. For triangular pulses of 2 ms duration, the presented impulse translates to a peak pressure of 150 MPa. On the other hand, under static loading, the lower head can take up to 50 MPa. For the actual material yield stress, all these values would have to be revised upwards by $\sim$40%.

The approximations of using an instantaneously delivered impulse, and the initial strain rate effect in Eq. (2), was tested with an ABAQUS shell-element model. Vice versa, the comparison helped in confirming the proper implementation of the numerical model. The model is illustrated in Fig. 4 and the material properties utilized in it are summarized in Table 1. The comparison of results with the predictions of the simple analytical model are shown in Fig. 5. The agreement is good and, as noted in the previous example, the strain rate effect is $\sim$50%. Also, it is interesting to note that the effect of finite (non-zero) impulse delivery time is non-negligible, and that the ideal impulse results are approached with the numerical model asymptotically.

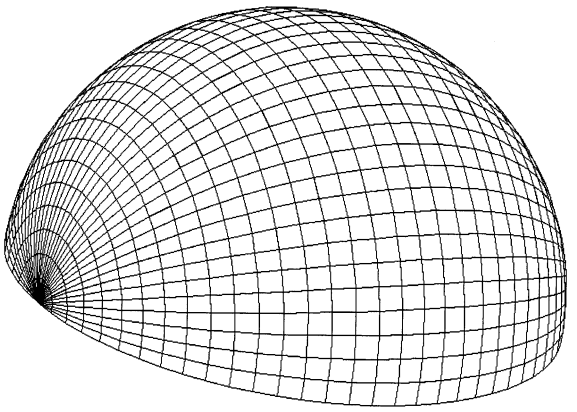

Fig. 4. Illustration of the shell-element ABAQUS model used in the comparisons of Fig. 5. The sphere inside diameter is 4 m, and wall thickness is 0.15 m.

It is clear, then, that Fig. 5 contains the essential features of the problem, for uniform impulsive loading, and hence we can define a 'characteristic impulse'

$$I^+ = \{2\rho\sigma_{y_o}^D\}^{1/2}\delta \quad (4)$$

and through it obtain the basic scaling law

$$\varepsilon = I^{*2} \quad (5)$$

with

$$I^* = \frac{I}{I^+} \quad (6)$$

Table 1
Material properties used in the calculations

Static yield strength (MPa)	330
Modulus of elasticity (GPa)	198
Density (kg/m^3)	8000
Strain rate hardening parameters D/p (s^{-1}/–)	40.5/5

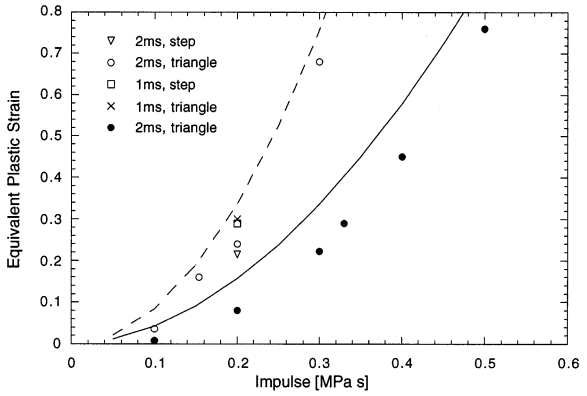

Fig. 5. Comparison of numerical results (points) with those of an ideal, instantaneous, impulse (lines). Solid lines and full circles are with strain rate effects and broken lines and all other points are without. The dynamic yield stress is based on the initial strain rate in the analytical model, and on the instantaneous value in the numerical model.

In these terms, the results of Fig. 5 can be recast as in Fig. 6, where we can more clearly see that as the dimensionless impulse increases, actual strains approach those due to an ideal impulse.

The effect of load localization was examined by means of the same shell-element model (Fig. 4), strain rate effects included. The loadings were applied as triangular pulses, over various fractional areas, as summarized in Table 2, with the pressure on the outer ring kept always to one-half of that on the disc, with the exception of one run, in which the same pressure was applied to the inner disc and outer ring. The results are summarized in Fig. 7. As expected, the greater the load localization, the greater is the reduction in the magnitude of the effective impulse, i.e. the work going into plastic deformation in the area of peak equivalent plastic strain. The difference goes, through load redistribution (bending moments), to plastic deformations in surrounding areas of the spherical shell.

On the way to generalizing this behavior, it is interesting to examine closer the complete plastic deformation distributions obtained under different loading patterns. The necessary data are provided in Figs. 8–10, which show representative trends from all the calculations performed. Beginning with Fig. 8, we can see that the maximum strains are always on the outside, and always at the apex of the loaded area. On the other hand, for all but the largest loading pattern, the inner wall is seen to experience maximum strains in the area peripheral to where the peak load is applied, and this is clearly due to bending, needed to accommodate the deformation between the peak loaded material and the surrounding material that is 'holding'. For pattern 3, the deformation at the periphery of the loaded area can be accommodated without pronounced bending, as it follows the natural curvature of the shell. Thus, highest strains on the inner wall for this case also occur at the apex of the loaded area. Also, it is interesting to note that the highly localized bending, in the more localized load areas, becomes more diffuse

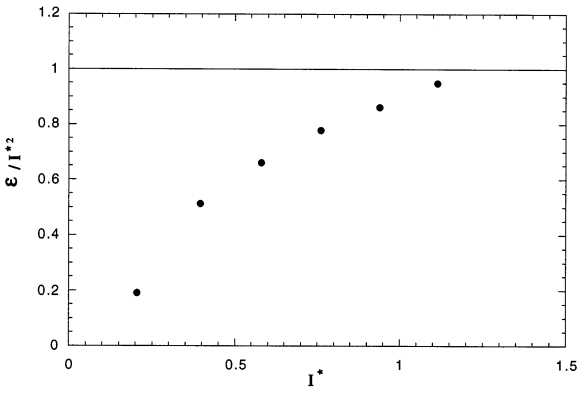

Fig. 6. The strain rate dependent results of Fig. 5 recast in dimensionless coordinates suggested by Eqs. (5) and (6), shown as a solid line.

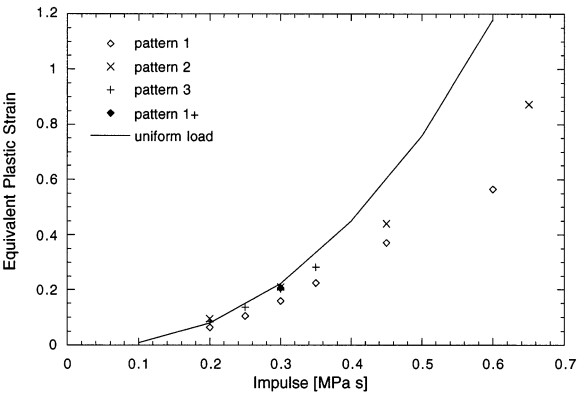

Fig. 7. The effect of localized loading on peak plastic equivalent strains.

Table 2
Loading patterns and respective dimensions for the non-uniform loading runs

Table 2 Loading Patterns and Respective Dimensions for the Non-Uniform Loading Runs

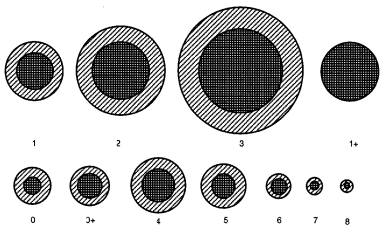

Loading Patterns	d_i^* (m)	d_o^* (m)	A_i (m^2)	A_o (m^2)	$\frac{2A_i}{\pi D_s^2}$ (%)	$\frac{2(A_i+A_0)}{\pi D_s^2}$ (%)
1	0.94	1.40	0.70	0.84	2.8	6.1
2	1.40	2.00	1.54	1.60	6.1	12.5
3	2.10	3.10	3.60	4.00	13.8	29.7
1+	1.40	—	1.54	—	6.1	—
0	0.39	0.87	0.12	0.47	0.5	2.3
0+	0.55	0.94	0.24	0.46	1.0	2.8
4	0.81	1.33	0.52	0.87	2.0	5.5
5	0.61	1.09	0.29	0.64	1.2	3.7
6	0.38	0.61	0.11	0.18	0.4	1.1
7	0.19	0.38	0.028	0.085	0.1	0.4
8	0.14	0.31	0.015	0.075	0.06	0.36

* Based on areas, i.e. $A_i = \pi d_i^2/4$, $A_o = \pi d_o^2/4 - A_i$

Loading patterns	d_i* (m)	d_o* (m)	A_i (m^2)	A_o (m^2)	$2A_i/\pi D_s^2$ (%)	$2(A_i+A_o)/\pi D_s^2$ (%)
1	0.94	1.40	0.70	0.84	2.8	6.1
2	1.40	2.00	1.54	1.60	6.1	12.5
3	2.10	3.10	3.60	4.00	13.8	29.7
1+	1.40	–	1.54	–	6.1	–
0	0.39	0.87	0.12	0.47	0.5	2.3
0+	0.55	0.94	0.24	0.46	1.0	2.8
4	0.81	1.33	0.52	0.87	2.0	5.5
5	0.61	1.09	0.29	0.64	1.2	3.7
6	0.38	0.61	0.11	0.18	0.4	1.1
7	0.19	0.38	0.028	0.085	0.1	0.4
8	0.14	0.31	0.015	0.075	0.06	0.36

* Based on areas, i.e. $A_i = \pi d_i^2/4$, $A_o = \pi d_o^2/4 - A_i$.

and less pronounced as the loaded area increases. Finally, by comparing the results of patterns 1 and 1+, it can be seen clearly that the details of loading pattern really do not make much difference. Moreover, very similar deformation distributions are obtained even under varying impulses.

The through-the-wall strain patterns relative to Fig. 8 are illustrated in Fig. 9. It is very interesting here to see the significant radial and angular gradients in strains, and that radial uniformity (i.e. the uniform loading result) is approached as the load area increases. Finally, the strains superposed on the actual deformation, for two sample cases, are shown in Fig. 10.

We attempt to quantify the effect of localized loading in the following manner. First, when the load is localized, part of the impulse has to go into bending energy around the periphery, so that the peak deformation is affected by a reduced impulse, and, making use of Eq. (2), we have

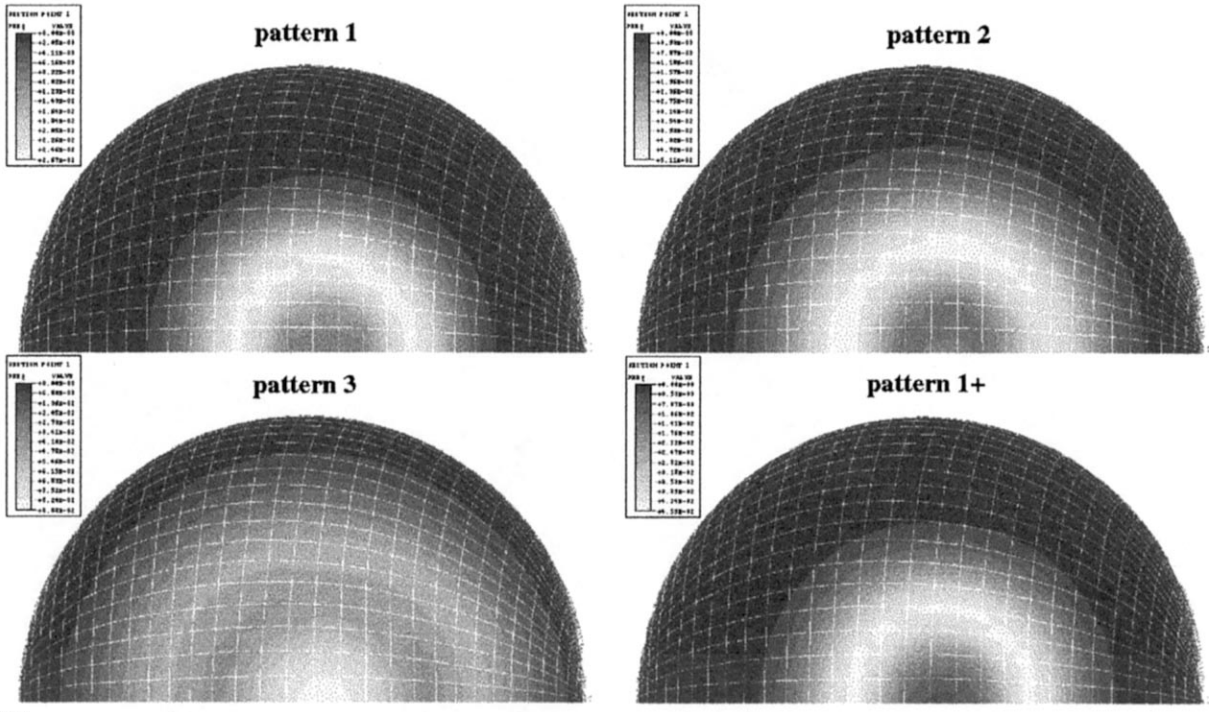

(a)

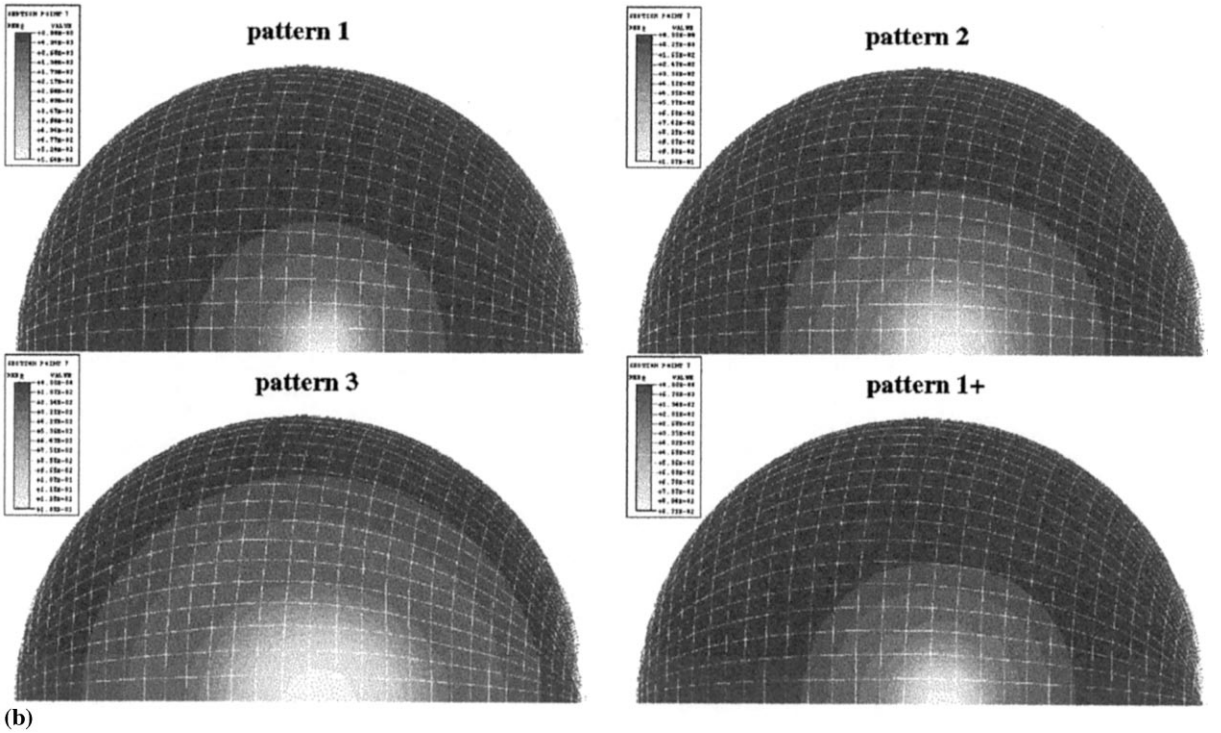

(b)

Fig. 8. (a) Equivalent plastic strain maps for a 0.3 MPa s impulse and different loading patterns: inner fiber. (b) Equivalent plastic strain maps for a 0.3 MPa s impulse and different loading patterns: middle fiber. (c) Equivalent plastic strain maps for a 0.3 MPa s impulse and different loading patterns: outer fiber.

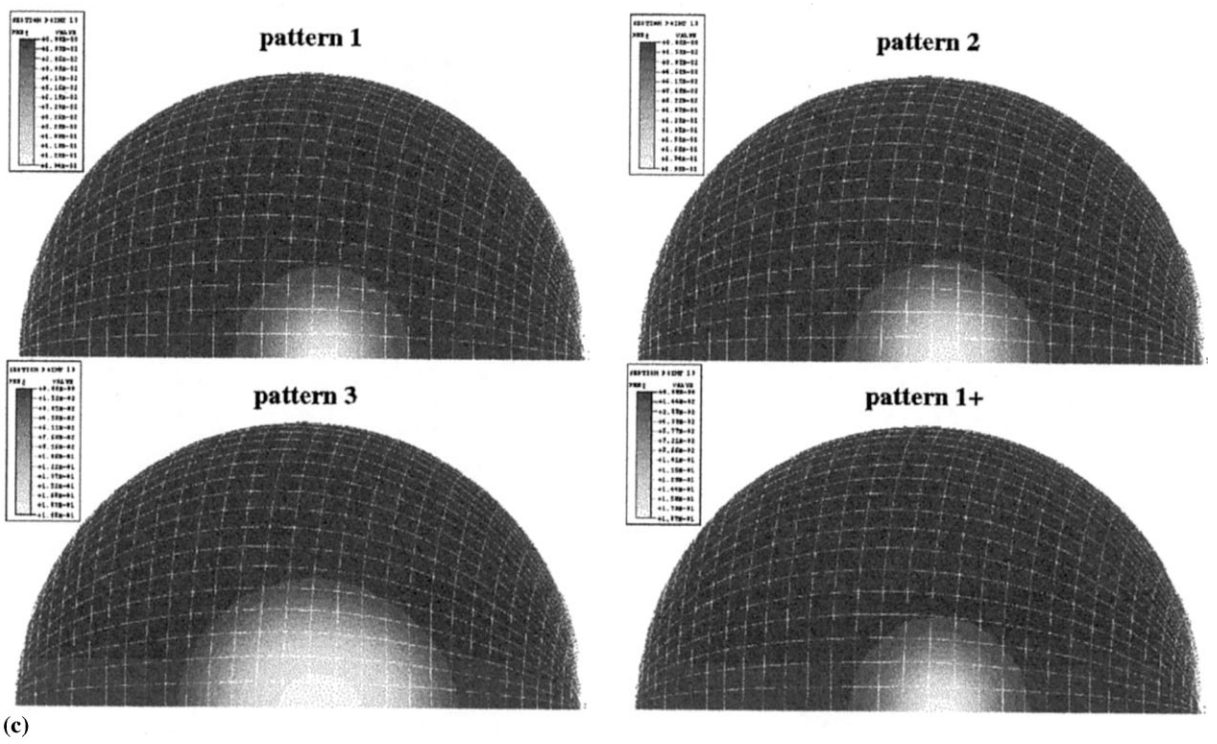

Fig. 8. (*Continued*)

$$\varepsilon_{3D} = \frac{(I - I_b)^2}{2\rho\delta^2\sigma_y^D} = \frac{I^2}{2\rho\delta^2\sigma_y^D}\left(1 - \frac{I_b}{I}\right)^2 = \varepsilon\left[1 - \frac{I_b}{I}\right]^2 \tag{7}$$

Second, we suppose that the fractional impulse energy dissipated in bending is inversely proportional to the fractional area loaded, and it is directly proportional to the magnitude of the impulse itself (to account for the non-linearity evident in Fig. 7); i.e.

$$\frac{I_b}{I} = \beta I \frac{D_s^2}{d_0^2} \tag{8}$$

where β is a material and geometric 'constant'. Thus, we can define an 'effective impulse' by

$$I_e = I - I_b \tag{9}$$

and Eq. (7) becomes

$$\frac{\varepsilon_{3D}}{\varepsilon} = \left(\frac{I_e}{I}\right) = \left\{1 - \beta I \frac{D_s^2}{d_0^2}\right\} \tag{10}$$

As seen in Fig. 11, this simple approach is able to properly scale the effect of load localization over a rather wide range of conditions.

A convenient to use rendition of Eq. (10) is given in Fig. 12. This figure can be used, in conjunction with Fig. 7, as a screening tool to determine whether a particular load merits further consideration. It will therefore be referred to as 'screening fragility', and its actual use is demonstrated at the end of Section 6. For loads that are deemed to be potentially significant (i.e. those that cannot be screened out readily on this bases), we need to consider in more detail actual failure mechanisms and respective criteria. This topic is addressed in the next section, and the result is used in combination with the detailed strain results found in the ABAQUS calculations, to come up with a proposed fragility of the lower head, for the class of loads pertinent to energetic steam explosions.

3.2. Failure criteria and fragility

Failure criteria for ductile materials, as is the

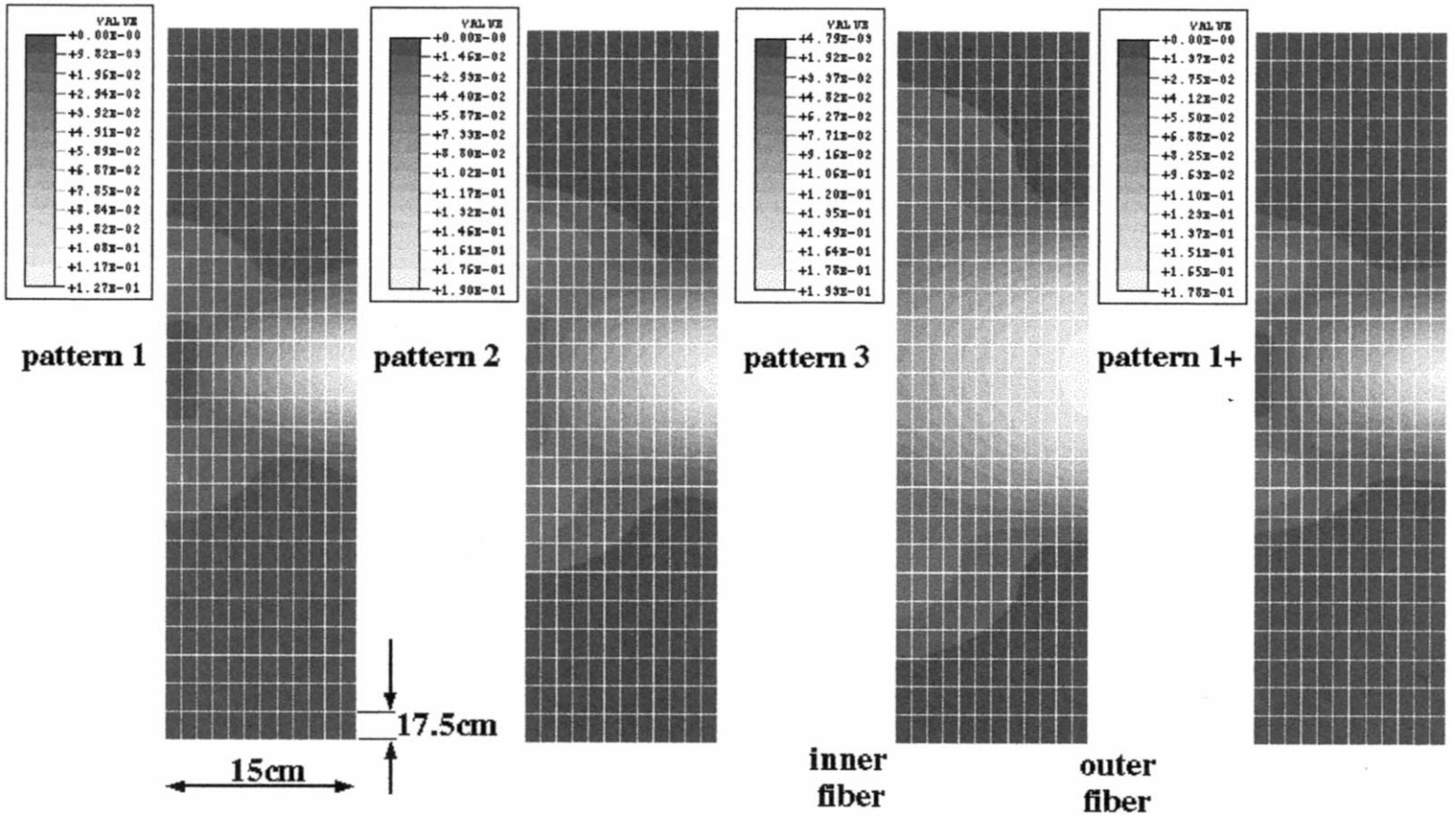

Fig. 9. Equivalent plastic strain distribution through the section of the shell for a 0.3 MPa s impulse and different loading patterns. The grid is not to scale.

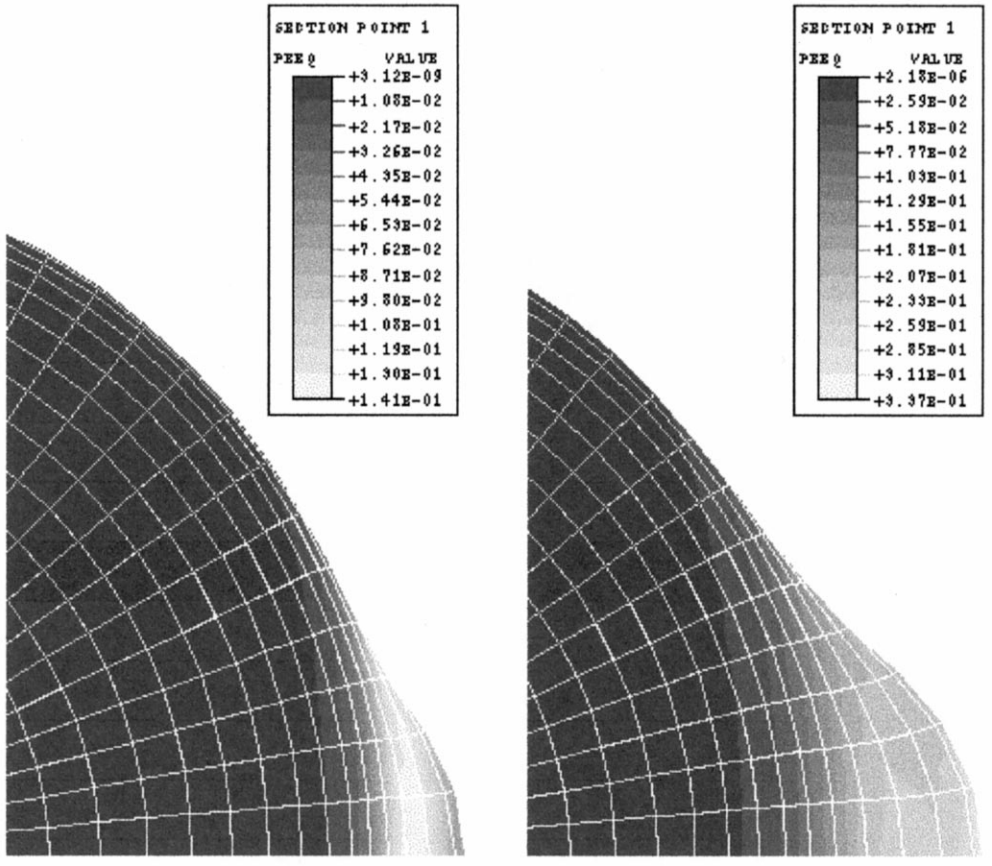

Fig. 10. Deformed geometry and map of equivalent plastic strains at the inner fiber under 0.6 MPa s impulse for patterns 1 (left) and 2 (right).

case here, have most commonly been based on plastic equivalent strains, with typically conservative 'ball park' values in the 12–18% range (Theofanous et al. 1987). All experimental evidence, however, and theoretical interpretations indicate that failures are not obtained until much greater strains, say in the 50–100% range.

For example, Olive et al. (1979) explosively loaded cylindrical shells made of a variety of metals (including mild steel), and observed strains-at-failure in the 70–90% range. Pao and Gilat (1992) tested A533B steel specimens and found that failure did not occur until strains exceeded $\sim 50\%$. Also with A533B steel, Shockey et al. (1980) found strains-at-failure in the 80–116% range. These results are particularly interesting because the A533B steel has only a slightly higher carbon content (0.19 vs. 0.16%), and a yield stress essentially equal to the as-tested value of the lower head material considered here.

The effect of stress anisotropy was evaluated by Korhonen (1987) on the basis of a metallurgical, plastic instability mechanism. Korhonen concluded that failure strain increases steadily from the isotropic value to nearly doubling as the principal stress ratio decreases to zero.

The potential effect of strain rate (on failure) has been examined with conflicting results. On the one hand, Johnson and Cook (1985) have provided an expression for the strain at failure (five material dependent parameters included) that indicates, in general, an increase with temperature and strain rate. On the other hand, Shockey et al. (1980) in the A533B tests already noted, explored

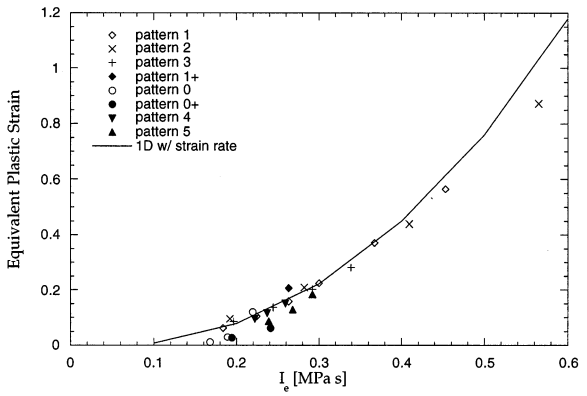

Fig. 11. Peak equivalent plastic strains as functions of 'effective impulse' for the class of loads relevant to the steam explosions considered in this work (from Eqs. (7) and (8), and $\beta = 0.05$).

strain rates of up to 1000 s^{-1}, and concluded that there are no effects of temperature or strain rate on failure.

In the absence of experimental evidence precisely on the steel of interest here, the failure criteria will have to be evaluated, conservatively, as an intangible. We make use, for this purpose, of the mechanistic ideas of ductile failure based on void nucleation, growth, and coalescence, and with particular reference to the work of Shockey et al. (1980). They found that voids nucleate predominantly on included particles, and that the threshold strain of 11% is needed for nucleation. This was also the strain at ultimate tensile strength corresponding to the onset of necking (in uniaxial test specimens). In applying these ideas to the present situation with a highly non-uniform distribution of plastic equivalent strains across the wall thickness, and recognizing that void coalescence (i.e. actual failure of the material locally) does not occur until strains of at least $\sim 80\%$, we take the approach that, conservatively, the global (wall) failure likelihood can be related to the fraction of the wall thickness experiencing strains that support nucleation, i.e. exceeding the 11% threshold. In particular, the four levels of likelihood (see Table A.1 in Appendix A of DOE/ID-10541) are applied to four wall-fractions affected by voids, as indicated in Table 3. The fragility is obtained by applying these criteria on an alternative presentation of the results shown in Fig. 7. It includes the 20, 40, and 60% 'boundaries', as

Table 3
Quantification of wall failure criteria

Likelihood	Wall fractional thickness (%) with plastic equivalent strain over 11%	Probability
Physically unreasonable	First Fiber	$<10^{-3}$
Outside spectrum	20	10^{-2}
Edge of spectrum	40	10^{-1}
Certain failure	60	10°

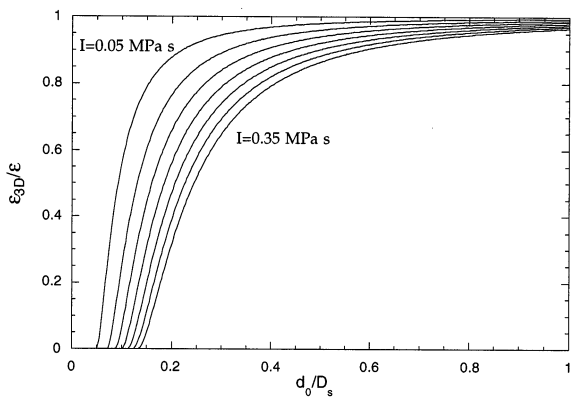

Fig. 12. The mitigative effect of localized loading as a function of the impulse applied and the degree of localization (from Eq. (10)).

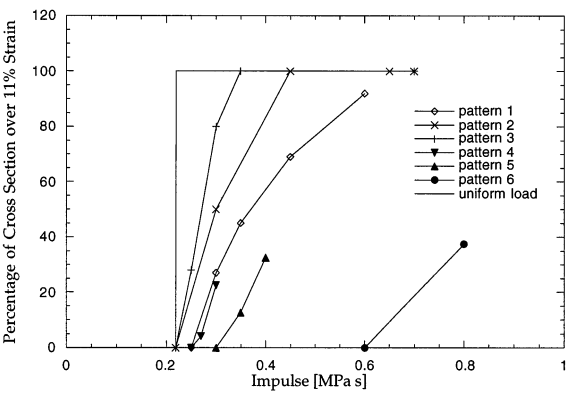

Fig. 13. Percentage of wall exceeding 11% strain as a function of impulse and loaded area.

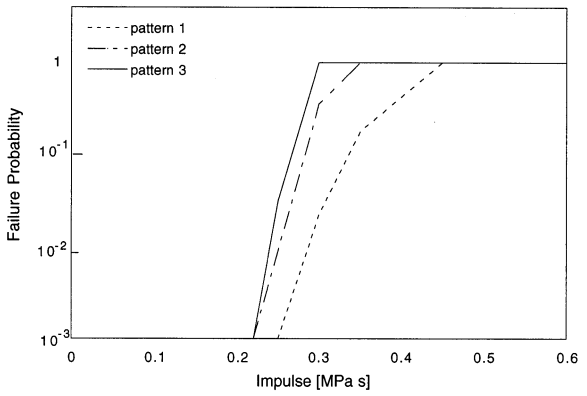

Fig. 14. Fragility as a function of loaded area.

shown in Fig. 13. The actual fragility is shown in Fig. 14. As the deformation depends also on the size of the loaded area, we have different fragilities for different loading patterns.

4. Quantification of melt relocation characteristics

Besides the low power density, the AP600 design differs significantly from current PWRs by having a substantial (~ 13 cm thick at the flats) stainless steel reflector as a core former, inside the core barrel (see Fig. 15). This reflector has a total mass of ~ 40 t, an 8% porosity due to cooling holes that run through its length, and it sits on the core support plate, which in turn is hung from the upper vessel flange as illustrated in Fig. 16. Its effect on the neutronics is to induce a much flatter radial power shape, as illustrated in Fig. 17, while its effect on the thermal hydraulics of severe accidents is to impose a very significant obstacle against a sidewards relocation of the core melt. On the other hand, as in all PWRs, core uncovery remains incomplete through the rapid oxidation phase, the lower portions of the core remain correspondingly cold, and there is a very significant heat sink associated with the core support plate (36 cm thick). In addition, in the AP600 there is an ~ 30 cm length between the bottom of the fuel pellets and the top of the core support plate, ~ 7 cm of which is occupied (within the rods, as illustrated in Fig. 18) by zirconium pellets (plugs)—an additional substansive heat sink. Thus, the downward relocation path for a melting core is formidable. We expect this path to be blocked by molten cladding and the blockage to be robust, especially as long as the core support plate is supported by the secondary support system from below (see support columns inside the lower plenum in Fig. 16).

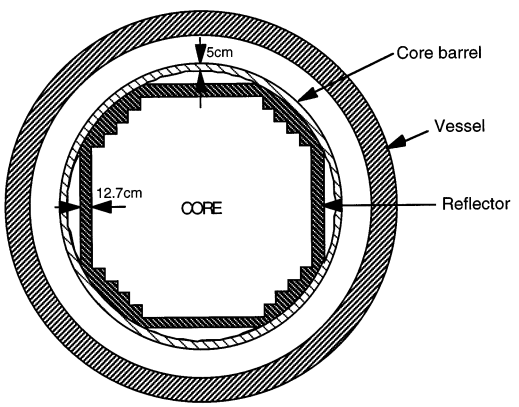

Fig. 15. Cross-sectional geometry of the reactor vessel and reflector.

As a consequence, the first relocation will occur after delayed failure of the reflector and core barrel at the upper end of the side boundary, and will be followed gradually by subsequent ones as the path opens more and more (downwards) by continued melting of the reflector and core barrel.

This is fundamentally different from what occurred in Three Mile Island (TMI), where a relatively small oxidic pool could melt through the relatively thin loaffle plate (of the core former), and discharge into the lower plenum through the so-called bypass region. Here there is no such 'open' bypass region, and the holes in the reflector will quickly plug as they become accessible to the melt. Also, the spaces between the flats and the core barrel in Fig. 15 are dead-ended at the bottom by the thick core support plate.

Around this pivotal idea, we outlined the basic features of the core relocation process and transition to the final bounding state in the IVR Report (Appendix 0.3). Here, we explore more deeply the early portion, up to the first relocation, relevant to the steam explosion problem. The key ingredients of this examination, which again is carried out on a basic-principles approach, are:

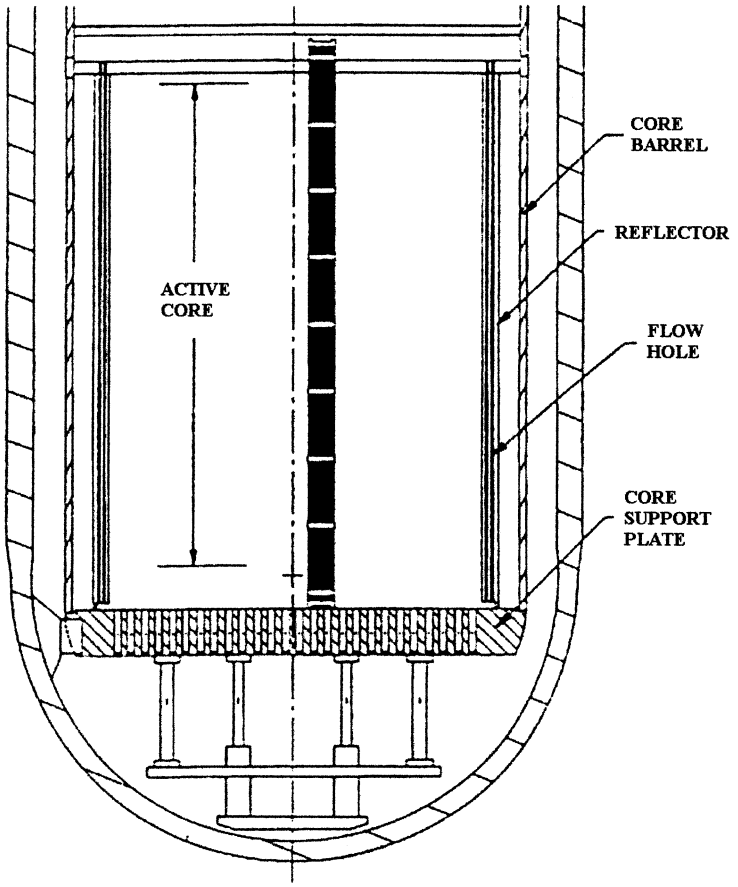

Fig. 16. Illustration of AP600 in-vessel structures.

- non-availability of a downward relocation path through the core support plate;
- molten pool formation and initial heat-up of reflector and core barrel; and
- melt-through of reflector and core barrel.

Each of these three main aspects of the first relocation problem is now discussed in turn. In particular, we show that lower blockage integrity is assured until well after the reflector and core barrel have failed. We conclude this section with the consideration of reflood scenarios, obtained as a consequence of the external flood level reaching the break elevation. We find that the core barrel cooling made available in such cases can arrest the melt attack, preventing failure, melt relocation, and potential steam explosions altogether.

4.1. Non-availability of downward relocation paths

Core materials relocate downwards as they melt. Leaving aside the low melting control materials that escape early, these downwards moving melts will consist initially of mainly metallic zircalloy at temperatures of ~ 2000 K, and will transition gradually to oxidic melts, i.e. ZrO_2 and ZrO_2/UO_2, at temperatures of ~ 3000 K. For all severe accident sequences of interest here, at the beginning of such melt motions, the core would be essentially, *but not completely*, uncovered, with the water level at $\sim 25\%$ of the active core height. This lower 25% of the fuel bundle, with its small internal characteristic dimension, and its large heat capacity constitutes an effective 'cold trap'.

A further cold trap, just below (see Fig. 18), is in the region of the lower Zr plug and lowermost spacer grid. The effectiveness of these cold traps can be very simply demonstrated, as given later. The ancillary consideration is that, once formed, such blockages will be sufficiently well cooled to maintain their structural integrity, i.e. avoid remelting. This is also demonstrated later.

4.1.1. Blockage formation

Consider the cold trap material consisting of solids with characteristic length scale d, and a volume fraction θ_s. A melt with negligible superheat, as is appropriate prior to the formation of a molten core pool, is allowed to flow through the open passages. Any crust forming is assumed to thermally equilibrate with the solids instantaneously. We are interested in estimating plugging times as a function of the initial solid temperature.

The energy balance on the solids is

$$\frac{d}{dt}(\rho_s\theta_s e_s + \rho_c\theta_c e_c) = \rho_m e_m \frac{d\theta_c}{dt} \tag{11}$$

where subscript s refers to the initially solid material and c to the crust, and e_m is the internal energy of the melt at its liquidus. The freezing rate, $d\theta_c/dt$, can be obtained from the rate of increase of crust thickness, δ_c, which is given by

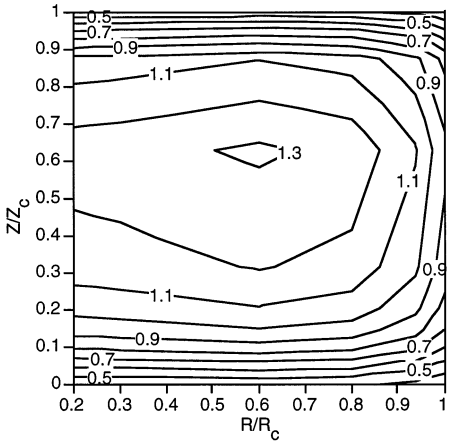

Fig. 17. The power distribution in an AP600-like core.

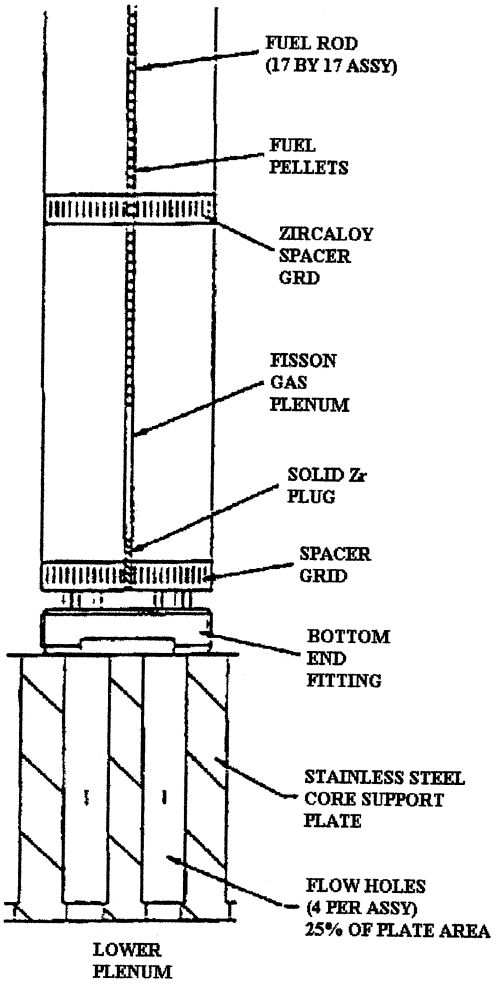

Fig. 18. Illustration of AP600 lower fuel assembly and core support plate features.

$$\frac{d\delta_c^2}{dt} = 2\lambda\alpha_s \tag{12}$$

where λ is the growth constant obtained for solidification in semi-infinite media (Carslaw and Jaeger, 1959). For a characteristic dimension equal to that of the fuel rod, the conduction time constant is of the order of 1 s, thus λ can be evaluated incrementally, while marching through the solution, with the current temperature obtained from Eq. (11). The solution is carried out until the frozen material obtains a volume fraction equal to that of the initial porosity, $(1-\theta_s)$.

Calculations were carried out for both metallic and oxidic melts, and for a range of initial fuel temperatures. The results are summarized in Table 4, and it is quite clear that even at temperatures significantly higher than those in the cold trap, the freezing and plugging process takes place in a matter of seconds. Clearly, the effectiveness of the second cold trap is also assured. These results are, of course, consistent with all previous experimental and analytical results, for current design PWRs. Most importantly, coherent, metallic lower blockages were also found in the TMI core post-accident examination.

4.1.2. Blockage coolability

A blockage formed in the lower extreme of the fuel bundle will be heated by the decay power under the axial flux shape factor of 0.4, which translates to a mean volumetric heating of ~ 0.5 MW/m^3 (the fuel volume fraction is $\sim 30\%$). In addition, it will receive a heat flux from the molten corium pool above, which could not exceed the fully-developed value of ~ 0.02 MW/m^2 (see next section). Cooling is provided from below, by radiation to water and/or the massive core support plate. We are interested to know whether this cooling is sufficient to allow that at least a few centimeters of this blockage remain below melting. This means temperatures below ~ 2800 or 2100 K for oxidic or metallic blockages, respectively.

The evaluation is carried out for a simple, one-dimensional conduction model, by specifying the blockage melting temperature and a heat flux of 0.02 MW/m^2 on the upper surface, and a radiation boundary condition at the lower surface. The effective conductivity is taken as the volume-weighted average of the constituents.

For radiation to water, the stable blockage thickness can be readily obtained from

$$L\dot{Q} + q_{dn} = f_r h_r (T_b - T_w) \tag{13}$$

where q_{dn} is the heat flux delivered from the molten pool, $\dot{Q}$ is the power density, and T_b is the lower end temperature obtained in combination with

$$\frac{1}{2}L\dot{Q} + q_{dn} = k\frac{T_{max} - T_b}{L} \tag{14}$$

and h_r is the radiation heat transfer coefficient given by

$$h_r = \frac{\sigma}{\frac{1}{\varepsilon_b} + \frac{1}{\varepsilon_w} - 1}(T_b^2 + T_w^2)(T_b + T_w) \tag{15}$$

In the calculations, we used $f_r = 0.7$, $\varepsilon_b = 0.75$, and $\varepsilon_w, = 1.0$, and obtained stable blockage thicknesses of ~ 10 and ~ 25 cm for oxidic and metallic blockages, respectively. Correspondingly, the radiative fluxes were ~ 0.1 and ~ 0.2 MW/m^2, and the lower blockage surface temperatures $\sim$ 1200 and ~ 1500 K.

This solution is applicable for as long as the lower core support plate is in contact with water. The relevant volume (between the bottom of the active fuel and the bottom of the support plate) is 4.1 m^3, and under the maximum radiative flux (0.2 MW/m^3), it would take ~ 100 min to vapor-

Table 4
Illustration of the cold trap effectiveness

Melt temperature (K)	Initial fuel rod temperature (K)	Final temperature (K)	Plugging time (s)	Melt freezing capacity as multiple of the fuel rod volume
Zircalloy 2100	1600	2056	8.9	1.5
	1400	1962	2.1	2.0
	1000	1798	0.8	2.8
	400	1628	0.6	3.6
UO_2 3120	1600	2910	9.5	1.4
	1500	2860	7.3	1.5
	1000	2610	3.4	1.9
	500	2360	2.4	2.4

ize this volume. In Section 4.3, we find that this time happens to be just about equal the time it would take to melt through the reflector and core barrel, and begin the relocation process through a sideways path. Once material is relocated into the lower plenum, the water vaporization rate will rapidly accelerate; however, the thermal inertia of the core support plate alone would be sufficient to provide an effective heat sink for a substantial additional time period.

Further insights on blockage formation and coolability can be found in the addendum to Chapter 4 of DOE/ID-10541.

4.2. Melt pool formation

While the actual melt attack on the reflector occurs well after the core pool forms, superheats, and begins to circulate, the period just prior to that is important, too, in establishing the thermal initial conditions. This is the melt pool formation period. It begins with core uncovery, and ends when a significant fraction of the fuel has reached its liquidus. The period itself consists of two thermophysically distinct phases. The first involves core heat-up past the rapid oxidation condition ($\sim$1500 K) and up to fuel melting temperatures ($\sim$3000 K), in an approximately as-is geometry, and is dominated by the heat of reaction, radiation heat transfer to the boundaries (reflector), and relocation of the metallic components (as they melt) to form the lower-end blockages as already discussed. The second phase involves melting and downwards slumping/draining of the oxidic components of the core (UO_2 and any remaining in place ZrO_2), and continuing heat-up towards a fully-developed molten pool. A fundamental point in examining these processes is that in the AP600, as already mentioned, the core power distribution is rather flat (see Fig. 17), and this allows considerable simplification in transitioning our analyses from one phase to another, and eventually to the treatment of the fully-developed pool which is provided in the next section.

4.2.1. Initial heat-up

We begin with the core essentially uncovered down to 20% of its height and at a temperature varying from 440 K at the bottom to $\sim$1500 K in the upper regions. For example, this corresponds to a time of 4500 s, immediately before the onset of rapid oxidation, calculated in a MAAP 4.0 run of the 3BE accident sequence (direct injection line break as discussed in the IVR Report). We neglect steam cooling effects (low pressure, velocity, and steam density), and are interested in computing heat-up due to the decay heat, and radiative losses to the boundaries. Heat-up of the reflector and core barrel are initiated at this time from a cold condition of 440 K. For this purpose, we employ a simple radial conduction model, with an effective thermal conductivity that properly represents interior (rod-to-rod) and boundary (rod-to-wall) radiation heat transfer. Axial effects are approximated by applying this model to horizontal slices of the core with the corresponding axial flux shape factor.

The effective thermal conductivity was obtained from the work of Manteufel and Todreas (1994) as

$$k_r = C_{rad}(4\pi d)\sigma T^3 \tag{16}$$

where the radiative coefficient, C_{rad}, is a function of rod emissivity and pitch to diameter ratio (1.33 for the AP600) as shown in Fig. 19. At the edge of the rod array, the temperature being T_e, the heat flux to a wall, at temperature T_w, is given as

$$q_r = h_e(T_e - T_w) \tag{17}$$

where

$$h_e = \frac{C_{rad,w2}}{\left(1-\frac{f}{2}\right)p}(4\pi d)\sigma\left(\frac{T_e+T_w}{2}\right)^3 \tag{18}$$

with

$$f = \frac{C_{rad,w1}}{k_r}(4\pi d)\sigma T_e^3 \tag{19}$$

The $C_{rad,w1}$, $C_{rad,w2}$ are the first and second wall coefficients, given as functions of the rod and wall emissivities as shown in Figs. 20 and 21, for the pitch-to-diameter ratios of interest here.

Zircalloy oxidation is represented by a specified fraction of the available reaction energy, released locally once the temperature reaches 1500 K. Based on a maximum adiabatic temperature in-

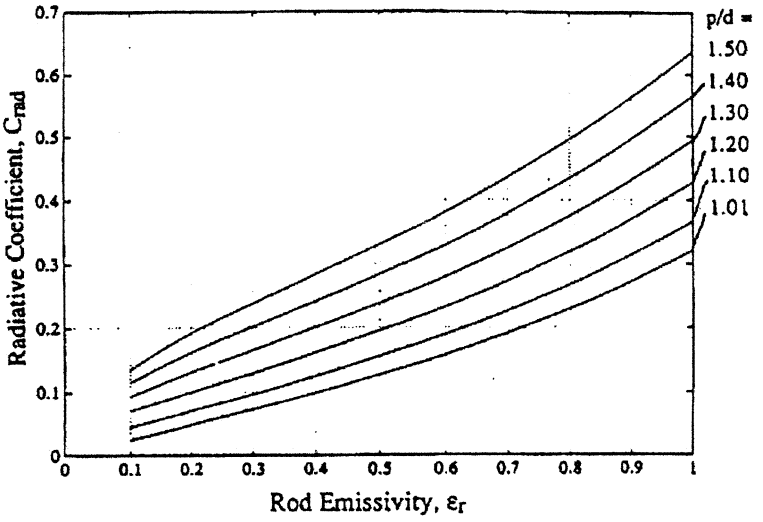

Fig. 19. Radiative coefficient appearing in radiative thermal conductivity for a square rod array (Manteufel, 1991).

crease of 1600 K, we use 640 and 1100 K corresponding to 40 and 70% extent of oxidation, respectively. The instantaneous release is reasonable, because in the rapid oxidation condition the heat-up rates reach ~ 10 K/s, so that the whole process is over in a matter of 1–2 min. Termination occurs locally as cladding melts and drains down. For comparison, outside this chemical regime, heat-up rates are one order lower, at ~ 0.5 K/s.

Calculations were carried out with a rod emittance of 0.8, and a reflector (stainless) emittance of 0.4. The radiation coefficient then is 0.375, and the first and second wall coefficients 0.189 and 0.154, respectively. The radial nodalization used encompasses 119 nodes in the core region, 40 (straight conduction) nodes in the combined reflector and core barrel region, and 10 nodes in the reactor vessel wall. The last two conduction regions were thermally coupled by a radiation heat flux boundary condition and emissivities values of 0.4.

The results are summarized in Figs. 22 and 23 for the 40 and 70% assumed oxidation, respectively, and they are quite similar, except for the expected acceleration in the latter case by ~ 600 s (the 500 K higher oxidation energy translates to ~ 600 s under decay power conditions). An axial perspective on these results can be obtained from Fig. 24. The key points of these results are twofold.

- One, that the rapid oxidation condition is mostly complete in about 600 s (~ 10 min), and that fuel melting temperatures are first reached in 30–40 min. For comparison, the MAAP calculation gave 45 min.
- Two, that the radial temperature gradient is limited to the outer 15 cm or so (i.e. to somewhat less than the outer row of fuel assemblies), while there is a significant heat-up of the reflector and the core barrel. Averaged over the heat-up period, this represents sinks of 3.3 and 0.73 MW for the reflector and core barrel, respectively; i.e. about 20% of the total core decay power at this time.

The axial perspective is particularly important for the reflector and core barrel regions, and is provided in Figs. 25 and 26, respectively. We see that melting is approached on the inner surface in the same time frame as melting of the fuel in the main part of the core. However, the rest of the mass and the core barrel are far from melting. Also, it is interesting to note the peaking over the central axial portion of the core height, and to realize that upon melting completely, the height of the core pool would be at ~ 1.8 m.

These time estimates can be verified by means of an overall energy balance. At the start of the

calculation (the 4500 s reference time noted earlier), the average core temperature is 1159 K, the 40 and 70% oxidation levels would bring it to 1800 and 2260 K, respectively, the decay power is 23.4 MW, and the power factor (upper 80% of the core) is 1.075. Assuming that the cladding drains to the bottom, the fuel heat-up continues under an effective power density (using the presented method and correcting for the losses) of 0.26 W/g, which yields ~ 0.5 K/s. Thus, to reach the solidus of the core fuel *as a whole*, we need 42 and 27 min for the two levels of oxidation considered, respectively. These times are comparable with those already estimated, although somewhat faster, but perhaps more appropriate, because the calculations presented here did not account for cladding draining.

4.2.2. Transition to a molten pool

As already found, the core approaches fuel melting temperatures, more or less uniformly, and within 27–42 min after uncovery (i.e. the 4500 s reference time from the MAAP calculation). At this time, the decay heat is 0.3 W/g of fuel, and complete melting (with a heat of fusion of 277 J/g) would require an additional ~ 15 min. What

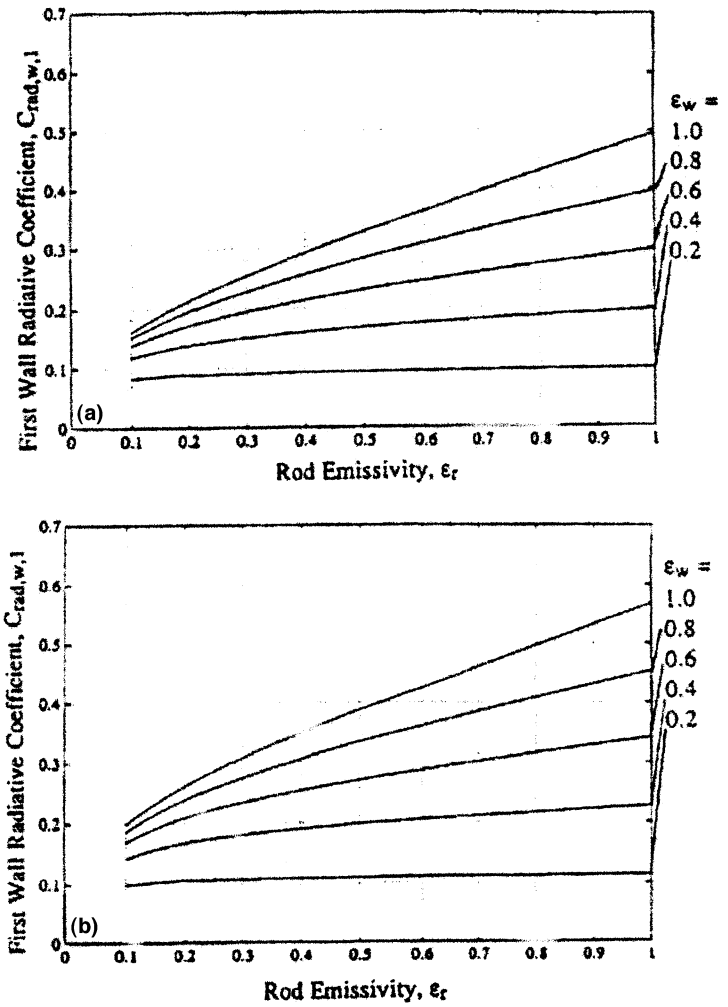

Fig. 20. (a, b) First wall radiative coefficient for square rod array with pitch-to-diameter of (a) 1.30 and (b) 1.40 (Manteufel, 1991).

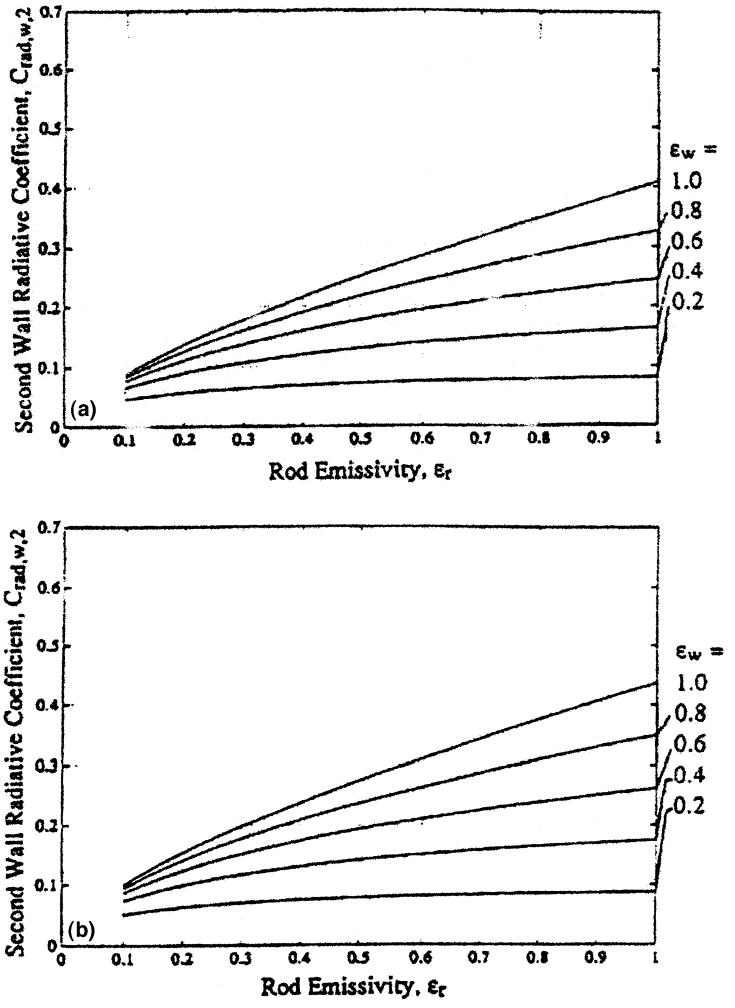

Fig. 21. (a, b) Second wall radiative coefficient for square rod array with pitch-to-diameter of (a) 1.30 and (b) 1.40 (Manteufel, 1991).

we need is an estimate of the additional heating at the reflector and core barrel during this 15-min transition period, so as to interface properly with the molten pool calculation in the next section.

The actual physics, during this period, is in fact quite complex, as the melt zone spreads out from the central regions (slight bias due to the flux shape peaking) towards the core periphery, characterized by freezing–melting cycles as molten material moves under gravity. Crusts build also in the radial periphery, and the radiation model used for the initial heat-up is expected to soon break down, as heat transfer control turns over to conduction through these peripheral crusts. Yet, the behavior can be bounded within a reasonably small range, sufficient for our purposes. On one hand, assume that the radiative heat-up of the reflector continues undiminished during this 15-min transition period. On the other hand, ignore any additional heat-up altogether. In the latter case, we initiate the molten pool calculation with the reflector and core barrel temperatures at 42 min of the initial heat-up calculation discussed earlier. This calculation also indicates a more or less uniform heating rate of these structures of ~ 10 K/min, which when applied to the former

case yields a temperature distribution raised uniformly by ~150 K. In the following, these two bounding behaviors will be referred to as 'with' and 'without' transition period heat-up.

4.3. Melt-through of reflector and core barrel

At this time, we are at 42–57 min from core uncovery, and no more than that from blockage formation at the lower end of the fuel bundle. This timing is significant in relation to the ~100 min estimated to vaporize the lower plenum water down to the bottom of the core support plate. What remains to be done now is to estimate the additional time it takes to melt through the reflector and core barrel, thus effecting the first relocation event into the lower plenum. In so doing, we will also have the melt pool conditions, as well as some perspectives on the possible location and size of the breech.

We approach the task by means of a model similar to that employed for the thermal analysis of the lower head in the IVR Report, but extended to account for the transient development of the melt superheat from an initial value of zero.

The pool is considered in the shape of an upright cylinder, with a nominal diameter equal to that of the reflector, and a height corresponding to the collapsed liquid level of the core contents, i.e. 1.8 m. The pool initially is at the liquidus of an oxidic melt taken as 80% UO_2 20% ZrO_2 by weight. As in the IVR Report treatment,

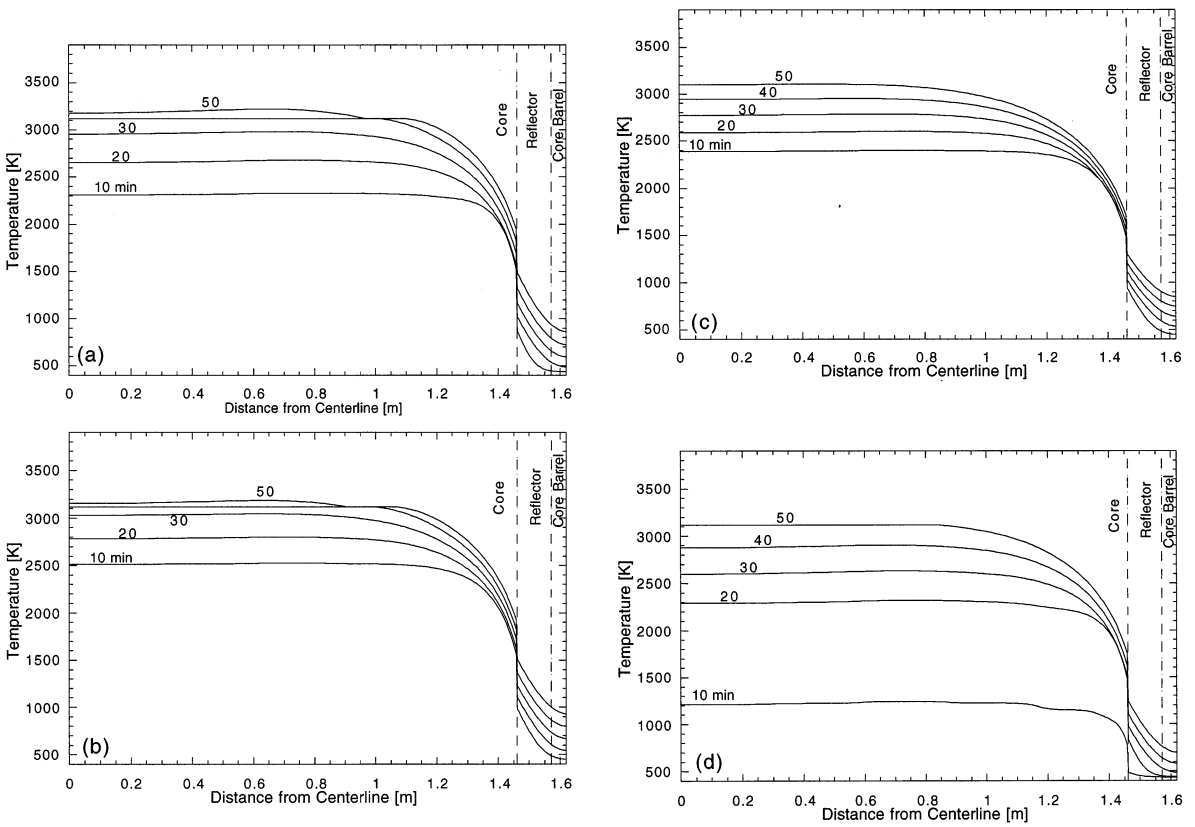

Fig. 22. (a, b). Radial temperature distributions in upper core during heat-up. Axial positions, normalized to core height, 0.6 (a), and 0.87 (b). Extent of oxidation 40%. (c, d) Radial temperature distributions in upper core during heat-up. Axial positions, normalized to core height, 0.94 (c), and 0.3 (d). Extent of oxidation 40%.

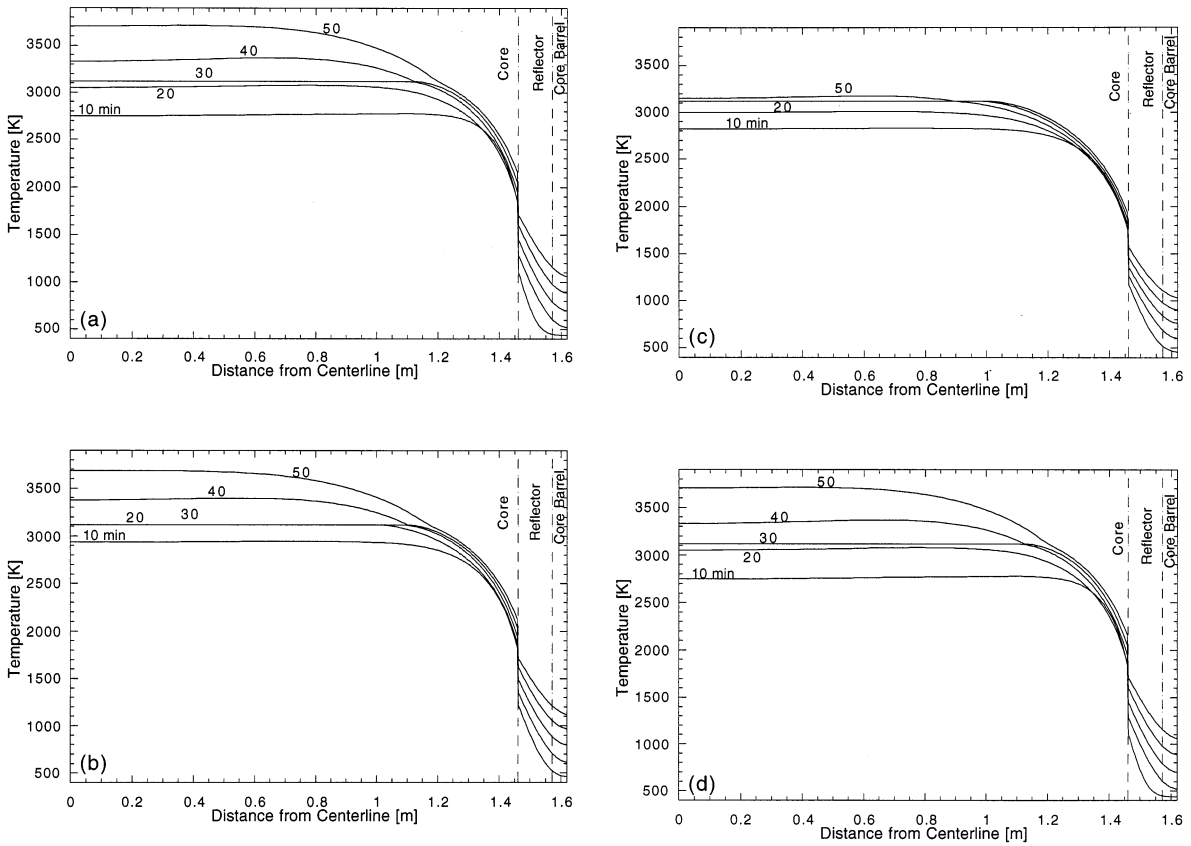

Fig. 23. (a, b). Radial temperature distributions in upper core during heat-up. Axial positions, normalized to core height, 0.6 (a), and 0.87 (b). Extent of oxidation 70%. (c, d) Radial temperature distributions in upper core during heat-up. Axial positions, normalized to core height, 0.94 (c), and 0.3 (d). Extent of oxidation 70%.

the oxidic melt is surrounded by crusts, and a metallic stainless steel layer is on the top. However, since here there is no cooling directly on the outside of the steel structures that contain the melt, we expect failure within a time frame for which the transient behavior must be accounted for. We need the unsteady energy balance for the melt, which can be written as

$$\rho_p \hat{c}_p \frac{dT_p}{dt} = \dot{Q} - \frac{1}{L_p}(q_{up} + q_{dn}) - \frac{2}{R_p} q_{hr} \tag{20}$$

where $\dot{Q}$ is the volumetric heat generation rate, L_p and R_p are the pool height and radius, respectively, and q_{up}, q_{dn}, and q_{hr} are heat fluxes in the up, down, and horizontal directions, across the respective cylinder surfaces. Also, we need an unsteady energy balance for the metal layer that accounts for mass addition from reflector melting (within the time frames of interest, melting of upper internal structures, by radiation off the top the metal layer, is negligible). That is:

$$\rho_l \hat{c}_l \frac{dT_l}{dt} = \frac{1}{L_p} q_{up} - \frac{2}{R_p} q_{l,hr} - \frac{1}{L_l} q_r - \frac{\hat{c}_l \dot{m}_l (T_l - T_m)}{\pi R_p^2 L_l} \tag{21}$$

where L_l is the transient metal layer height obtained from the reflector melting rate, $\dot{m}_l$ by

$$\pi R^2 \rho_l \frac{dL_l}{dt} = \dot{m}_l \tag{22}$$

$q_{l,hr}$ and q_r are the convective and radiative fluxes off the side and top metal layer surfaces, and the

last term in Eq. (21) accounts for the melt entering the layer at its liquidus. The reflector melting rate is obtained from transient conduction (as done in the initial heat-up phase in Section 4.2) under the heat flux q_{hr}, which is a function of axial position (and time).

As explained in the IVR Report, as long as the oxidic pool is surrounded by crusts, which is the case here, these two problems are basically uncoupled. We can thus readily solve Eq. (20) and quickly obtain the melt-through time at the top of the oxidic pool. Then we impose the q_{up} transient obtained into Eqs. (21) and (22) to solve for $q_{l,hr}$, which can be used to provide another estimate of the melt-through time—this time at the metal layer elevation. These procedures, some further details of the calculations, and the results obtained are summarized later.

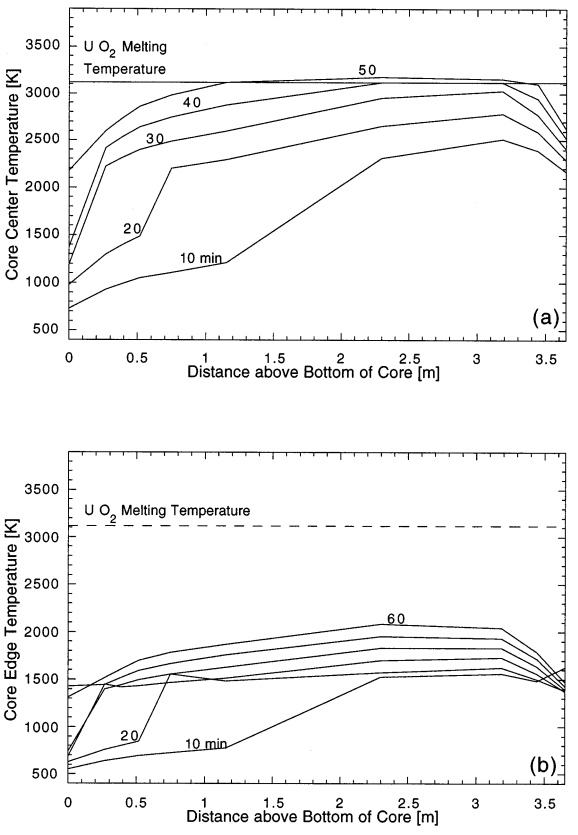

Fig. 24. (a, b) Axial temperature distributions during heat-up along the core centerline (a), and core edge (b). Extent of oxidation 40%.

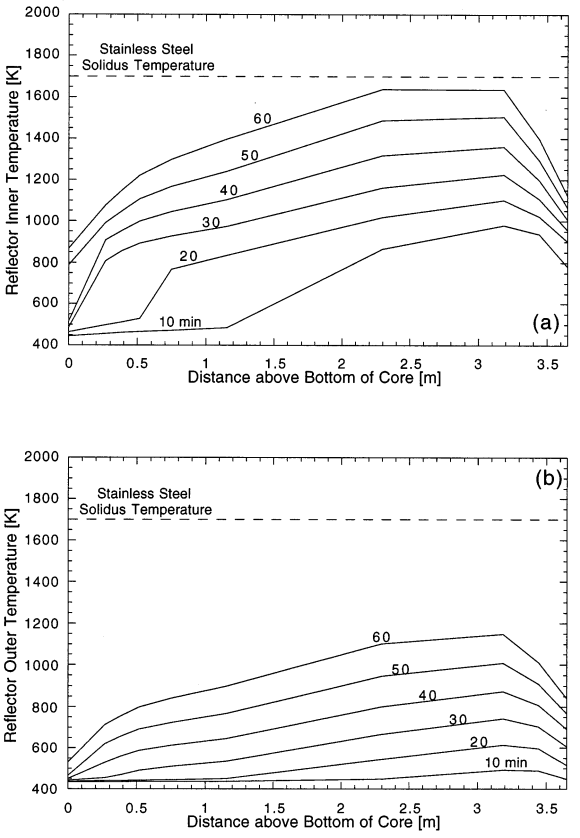

Fig. 25. (a, b) Axial temperature distributions along reflector inner surface (a), and reflector outer surface (b), during heat-up. Extent of oxidation 40%.

4.3.1. The oxidic pool

Eq. (20) was solved with all specifications as in the IVR Report. This includes: (a) decay heat, accounting for volatile losses, but evaluated at 2 1/4 h; (b) material and transport properties; and (c) the Steinberner–Reineke correlations for the heat fluxes at the boundaries.

In particular, we know that the data for these correlations were obtained in rectangular geometry, as is the case of interest here. The correlations are

$$Nu_{up} = 0.345\ Ra'^{0.233} \tag{23}$$

$$Nu_{dn} = 1.389\ Ra'^{0.095} \tag{24}$$

$$Nu_{hr} = 0.85\ Ra'^{0.19} \tag{25}$$

where the Nusselt and Rayleigh numbers are defined in the usual way (see Appendix A). It is also interesting to note that Eq. (23) was verified also by the mini-ACOPO data (see IVR Report), and that Eq. (25) is actually in good agreement with Mayinger's correlation, as it should be, applied to the top edge of a hemisphere through a peak-to-average factor of 1.5, i.e.

$$\mathrm{Nu}_{\mathrm{dn}}(\theta = 90^{\circ}) = 0.825\,\mathrm{Ra}'^{0.2} \tag{26}$$

Finally, it should be noted that Eq. (24) might exhibit some small sensitivity to the Prandtl number (Nourgaliev et al., 1997), but the contribution of this term is negligible not only to the pool, but also to the thermal loading of the lower blockage examined in Section 4.1.

The results are summarized in Fig. 27. In particular, note that within only 5 min, the pool superheat builds to $\sim$70 K and the heat flux to the reflector has already reached the radiative flux at the end of the initial heat-up period in Section 4.2 ($\sim$150 kW/m^2). The superheat builds asymptotically to $\sim$180 K and the sideways flux to $\sim$400 kW/m^2. Applying the actual flux history to the reflector, through the detailed conduction model and with an initial condition as described in Section 4.2, we obtain melt-through at 34 and 38 min for the two bounding cases denoted earlier as 'with' and 'without', respectively. Using an average flux of 150 kW/m^2, an initial average temperature in the reflector of 1500 K (see Fig. 22(a), plus the 150 K), a hand calculation also yields a failure time of 34 min. Thus, the approximation made for the transition period is confirmed to reasonably and narrowly bound the behavior.

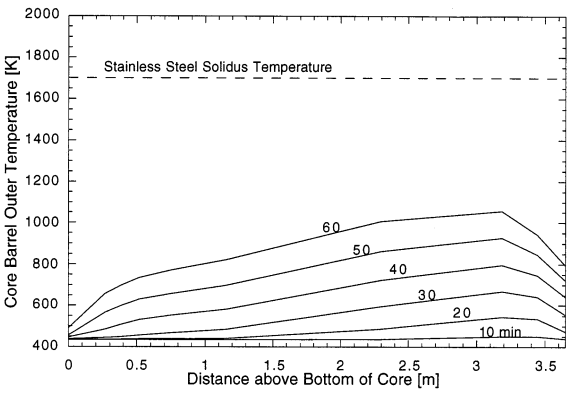

Fig. 26. Axial temperature distributions along the core barrel outer surface during heat-up. Extent of oxidation 40%.

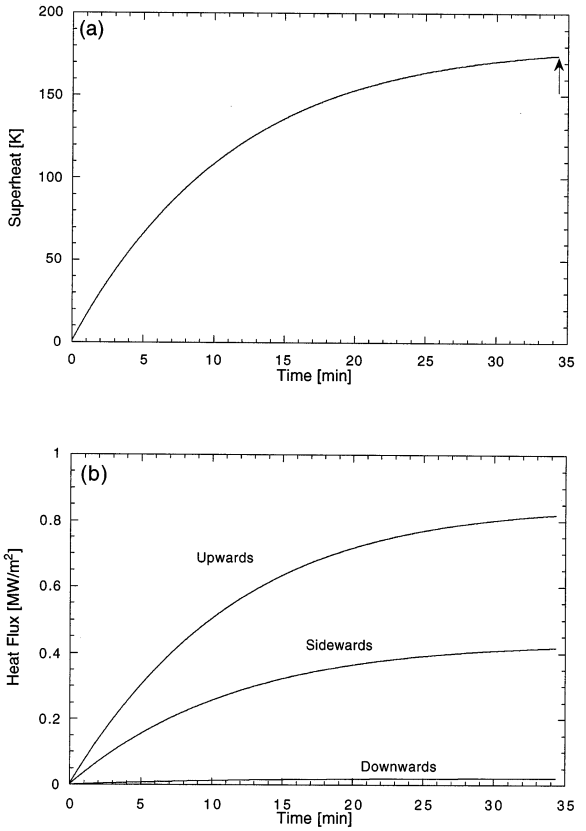

Fig. 27. (a) Development of melt superheat with time in the oxidic pool. The arrow indicates melt-through. (b) Development of heat fluxes to the boundaries of the oxidic pool.

4.3.2. The metal layer

Eq. (21) was solved with the $q_{\mathrm{up}}(t)$ value already obtained, and the q_{r}, $q_{\ell,\mathrm{hr}}$ terms modeled as in the IVR Report. The results are summarized in Fig. 28. We can see that the focusing effect described in the IVR Report is very important here, and that as expected, failure is obtained much sooner than that found for the oxidic pool. We can thus conclude that since the flats are to fail first (see Fig. 15), the metal will be gradually draining, as it becomes molten, into the spaces between these flats and the core barrel, where it is

resolidified, and that this will continue until the oxidic pool melts through the reflector. The total volume of these spaces, between the top of the core support plate and the pool surface, is 1.4 m^3, which can contain $\sim$10 t of steel (i.e. 25% of the total reflector, or $\sim$50% of the portion corresponding to the pool height).

4.3.3. Melt release conditions

The key conclusion of this is that when the oxide melts through the reflector, it has no metal layer on top of it. Moreover, failure of the already preheated core barrel will occur soon after that, and again with no significant quantity of metal on top. Thus, the release will be oxidic, with a superheat of $\sim$180 K.

The other key conclusion we can arrive at now is that the release will occur within 76–91 min from the rapid oxidation phase and formation of the lower blockage (42–57 min, plus the 34 min already found), and that this time frame is within the demonstrated coolability of the lower blockage (100 min to just vaporize the water to the bottom of the lower core support plate, and the massive heat sink of the plate itself thereafter).

Finally, for the failure itself, we can expect that it will be local azimuthally and very near the top of the oxidic pool. The azimuthal localization is imposed by the structural heterogeneity as seen in Fig. 15. For example, the flats length (along the azimuthal) is 1.4 m, and about one-third of this dimension would appear, geometrically a good upper bound on the first breech width. We will

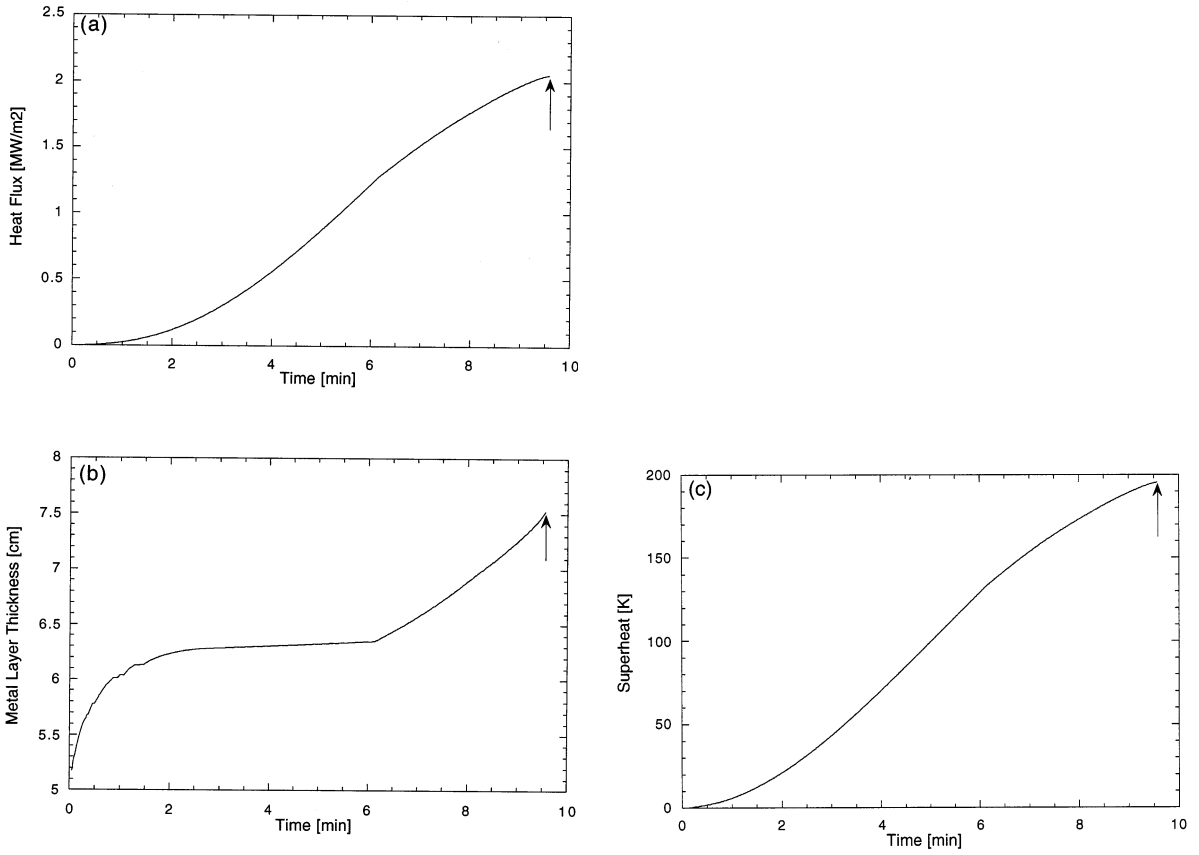

Fig. 28. (a) Development of heat flux to the side wall contact with the metal layer. Arrow indicates meltthrough. (b) Metal layer thickness increase with time due to the melt-in of reflector material. (c) Development of superheat in the metal layer.

use a dimension of 0.4 m for this upper bound (10^{-2} level of probability), and half of that (0.2 m) for an edge of spectrum value (10^{-1} probability). Axially, the location is biased very near the top, by the cumulative preheating of the core barrel in the initial heat-up transient (Fig. 26), and the higher heat flux region established by the focusing effect on the reflector (prior to its failure), and by the normally expected slight peaking of the heat flux from volumetrically heated pools on vertical walls (see Steinberner and Reineke, 1978; Kymäläinen et al., 1993, and the IVR Report). Also, the thickness of the core barrel itself (~ 5 cm) is relevant. We choose an ~ 10 cm axial gap, and believe that it is conservative. Under gravity draining, such a gap would produce an exit velocity of melt of 1 m/s, and a pour rate of ~ 100 kg/s per 10 cm of azimuthal breech dimension. Thus, the 0.2 and 0.4 m openings would release 200 and 400 kg/s of melt, and this appears to be a reasonable range physically to bound the behavior.

4.4. Consideration of reflood scenarios

As was the case for the IVR Report, in the course of this work, we interfaced with Westinghouse (J. Scobel) on systems aspects, especially the thermal hydraulics of overall scenario evolution, and identification of the plant damage states that belong to the severe accident management domain, or 'mitigation window' (Scobel et al., 1996). The Westinghouse work has been carried out with systems code MAAP4.0. Of particular interest to us here is to determine whether any conditions can develop, in a scenario sense, that could materially alter the core meltdown sequence developed.

Parenthetically, it is noted that the MAAP AP600 model being used by Westinghouse did not represent the reflector. As a consequence, it not only missed the ~ 30 min time needed to melt through the reflector, it took on a completely different path, by relocating portions of the core as they became molten (roughly in 20% intervals), thus bypassing the whole-core pool found in our assessment. This is not significant for the purposes of the discussion that follows.

Three passive reflood scenarios were identified. They will be called, 'fast', 'medium', and 'slow', respectively. The slow and medium ones arise from the water level rising to the top of the reactor vessel, under the operation of one or two lines of the cavity flooding system, respectively. The corresponding time intervals are 90 and $\sim$ 170 min. The fast scenario, on the other hand, arises when the break that caused the accident is in one of the two so-called valve rooms that house the two valves connecting the gravity flooding system to the reactor vessel. This is a very special scenario that requires one of the two valves to work (the one in the room where the break is), and the other to fail (the one in the other room) in order to have a severe accident in the first place. Vessel flooding begins when the water level, in the flooded room, reaches the break elevation, and this clearly depends on the drain size in the floors of these rooms. For example, for a drain size of 4 inches, reflood begins 15 min *prior* to the core reaching rapid oxidation temperatures, while for large enough drain areas, the time for reflood would approach those already quoted for the medium and slow scenarios. As one can deduce from the following, this 'fast' reflood is adequately enveloped for our purposes by the medium scenario, and it needs no further explicit consideration.

Recalling now the timing of core barrel melt-through as ~ 90 min, we recognize that in slow scenarios, reflooding would occur more than 1 h later (~ 170 min). Thus, the basic melt progression and core relocation behavior can be considered to remain unaffected along the lines considered earlier in this section and in the IVR Report. The refined timeline, as illustrated in Fig. 29, shows additional margins from an IVR point of view; i.e. to externally flooding the reactor vessel prior to the initiation of core relocation. On the other hand, the medium scenarios, and certainly early scenarios of the type discussed here, present the possibility of flooding (at ~ 90 min) prior to core barrel failure (see Fig. 29), and this would lead to the kind of 'departure' we set out looking for in this section. It is an interesting departure, indeed.

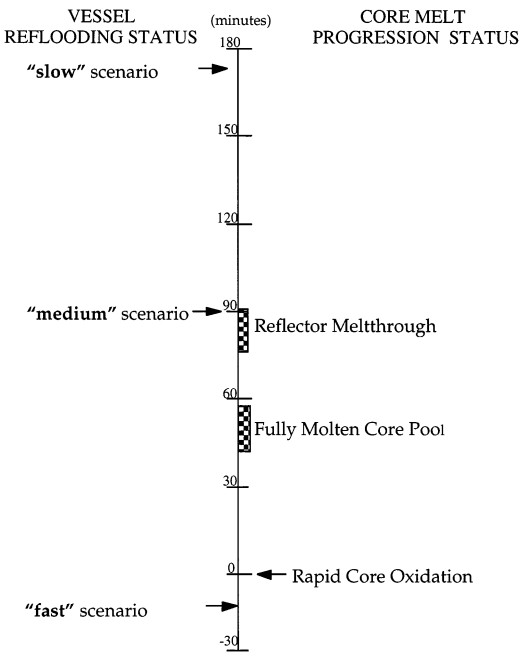

Fig. 29. Timing in reflood scenarios.

The 'new' situation involves a convecting oxidic pool, contained by the core barrel (and the remains, as solid, parts of the reflector) which is cooled on the outside by a churning steam–water mixture. As found in Section 4.3, the nominal thermal load created is ~ 400 kW/m^2, and we expect this load to be readily accommodated by radiation and film boiling heat transfer on the outside. For example, just radiation heat transfer would require an external (core barrel) surface temperature of ~ 1600 K, while with film boiling the surface temperature may be as low as ~ 1400 K (Okkonen et al., 1996). Moreover, we can expect a quench front to propagate from the bottom end (which is at relatively low temperatures) upwards, eventually quenching the whole outside. This process would be further aided by coolant flow through any yet-unmelted reflector holes, eventually leading to water release into the upper plenum and quenching of the top surface of the melt also. As discussed extensively in the IVR Report, failure under these conditions can be obtained only through a potential focusing mechanism due to thin metal layers on top of the oxidic pool. In the present case, such conditions are not as easy to exclude, however, as was the case for IVR; such local failures do not jeopardize the retentive property of the containing structure as a whole. Rather, they would allow water to ingress, flooding the top of the melt and arresting the whole melt attack process (Theofanous et al., 1995a). Also note that in the present case, the molten steel escapes into the gaps behind the reflector, as noted already, and that focusing, if any, would occur only after these gaps have been filled (this requires about 25% of the whole reflector volume, or about 50% of that below the pool level), and from a real thin layer in the early stages of its formation.

Thus, we conclude that the reflood scenarios need no further consideration from a steam explosion (lower head integrity) standpoint. Moreover, and interestingly enough, such reflood scenarios would provide further margins (other than those shown in the IVR Report) to thermally challenging the integrity of the lower head.

5. Quantification of premixtures

In the previous section, we found that the first release will involve an oxidic melt with a superheat of ~ 180 K pouring into the downcomer and through it into the lower plenum at rates in the range of 200–400 kg/s. At that time, the water will be saturated, and with its level somewhere between the bottom of the active core and the bottom of the lower core support plate, as shown in Fig. 30. We are interested, here, to determine the range of premixtures possible; i.e. the space–time evolution of melt, water, and steam volume fraction distributions created as the melt penetrates towards the bottom of the lower head. Also, we are interested to know the distributions of the melt length scales, and as remarked already, the relationship between these length scales and the degree of voiding obtained in the premixture.

The most remarkable feature of this problem is its highly three-dimensional character. In one respect, depending on its velocity, the melt may come down along the inside of the vessel wall, and

descend following the contour of the lower head, except for possible disruptions of this stream by freezing and/or splattering from the wall, and vaporization of water trapped in between. On the other hand, because the water is saturated, we expect that this mixing process will produce copious amounts of vapor, which would also have a disrupting influence on the melt as soon as the leading edge of it contacts water. Finally, it should be clear also that the mixing region would evolve under the 'pinching effect' at the lower core support plate proximal area with the lower head, and in one azimuthal location (i.e. 'one corner', so-to-speak, of the lower plenum).

Specifically for this work, therefore, the original 2D PM-ALPHA code was extended to three dimensions. This new tool (called PM-ALPHA-3D), which also involves improved numerics, has been verified by extensive comparisons, on 1D as well as axisymmetric problems (run in 3D), with PM-ALPHA. The PM-ALPHA code, in turn, has been verified extensively by comparison with a comprehensive set of experiments and analytical solutions as documented in a special verification report (Theofanous and Yuen, 1998b). In the course of the work, we also developed PM-ALPHA.L-3D, which utilizes a Lagrangian formulation for the fuel particles and thus eliminates numerically induced mixing. Results from this more accurate tool are also included.

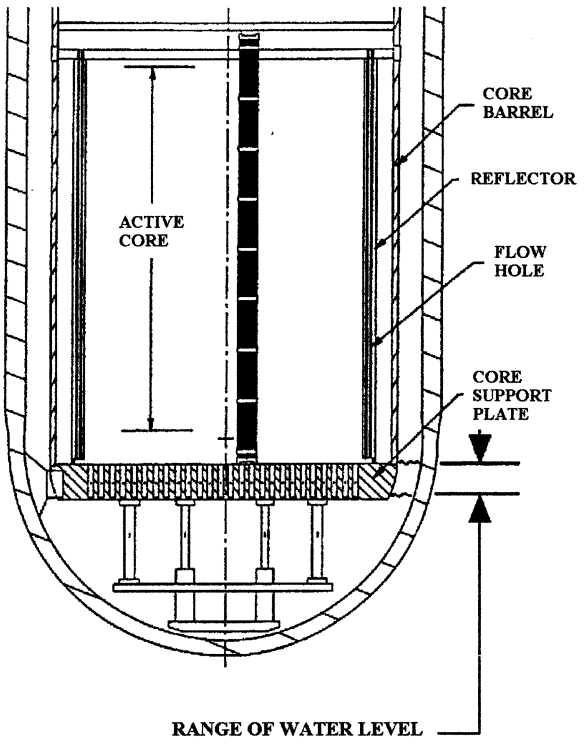

Fig. 30. The range of possible water levels in the lower plenum.

Briefly, our verification approach is based on a 'fitness-for-purpose' attitude. Specifically, the main focus is to exhaustively explore, and verify, the multifield aspects; that is, all aspects of the computation except melt break-up. In particular, we use for this purpose fundamentally oriented experiments that allow unambiguous predictions (all conditions well specified) and detailed comparisons with experimental data (i.e. premixture internal void fractions). Also for this purpose, we use an array of analytical solutions. On this solid base, we then approach break-up behavior, approximately, by comparison to integral experiments, and in reactor calculations by exploring parametrically the effect of various degrees of break-up. As we show later, these effects can be adequately bounded.

Calculations were carried out for the conditions already described, at the two flow rates of 200 and 400 kg/s. The computer runs were denoted as C1 and C2, respectively. The melt was released at the 1.8 m elevation (above the water level), with an initial velocity of 1 m/s, and was allowed to accelerate under gravity, reaching ~ 5 m/s upon entering the water. Radially, the melt was distributed over an effective radial width of 10 cm ($\sim 1/2$ the downcomer gap), and the initial melt fraction was specified such as to produce the proper total flow rate. Due to acceleration, this volume fraction reduced to $\sim 25\%$ at water impact. Our principal interest was to bound the effect of break-up (as described already), and on this task we proceeded as follows.

To begin with, we chose a melt drop length scale of 20 mm as a large enough value to represent a minimally broken-up melt stream. We then carried out a series of preliminary scoping calculations on a coarse, 10 cm (on the side, cubic) grid,

with the break-up parameter varying over 10, 12.5, 15, 20, and $\beta \to \infty$. The value of 10 produces a very rapid break-up, down to ~ 2 mm within a very short travel distance in water (~ 10 cm); the very large value ($\beta \to \infty$) yields no break-up at all; and the intermediate break-up states are obtained from the other values. As expected from our previous experience, we found extensive voiding (water depletion of the premixtures) developing rather rapidly in all cases, the rate of voiding increasing rapidly with the rate of break-up. These scoping results were then subjected to triggers, as detailed in the next section, so as to develop a qualitative 'feel' of the effect of voids on the severity of the explosion. On the basis of this background, we then proceeded to specify a final set of calculations, which could comprehensively reflect the range of behavior. They included three values of β, 10, 20 and ∞, and two grid sizes, 10 and 2 cm. The runs were denoted by attaching the value of β (except for $\beta \to \infty$, denoted by 'nb') to the C1 or C2 designation. The high resolution (2 cm grid) runs are denoted with the prefix R. The fine resolution grid was deemed indispensable, mainly because of two reasons; first, to properly represent the curving lower head boundary, especially in the important region where it is first encountered by the melt; and second, to better represent the melt stream itself as it is being deflected by the curved boundary (both of these issues were further resolved by the use of PM-ALPHA.L, as described later).

The results are presented in four different, successively more integral, formats; namely, detailed 3D evolution of the volume fractions, area-average volume fraction distributions along the length of the melt trajectory, volume-integrals of the quantity of melt that is in contact with coolant in a given void fraction range, and finally, a θ_f–α map sequence based on which one can visualize the extent of spatial volumes involving fuel and water together with the corresponding fuel length scales. Each of these groups of results is presented, in turn.

The detailed, 3D behavior was visualized with C2 runs, taken at the two extremes of break-up. These runs are summarized in Part 1 of Appendix B of DOE/ID-10541, and a sample is provided in Fig. 35. This figure, in particular, shows the melt-stream/wall interactions and resulting highly dynamic material distribution patterns, the continuing nature of this interaction under the deflecting effect of the curved wall, the presence of non-voided premixtures at the leading edge in the absence of break-up, and the long-term lower plenum voiding patterns. Also, it is interesting to note the steep water-to-void boundaries created at the premixture edges, even in the absence of break-up. Given the near-wall, dense-melt configurations observed, mention should be made of the PMALPHA model, making use of an effective packed bed concept. Ignoring coalescence, this is an approximate treatment that is expected to be adequate for our purposes; i.e. properly representing an effectively separated melt layer, void of any coolant. Perhaps more importantly, this condition is approached under reasonably appropriate laws for drag and heat transfer. On balance, it should be noted that some experimental insights on this sort of stream/wall interaction would be welcome, and that such work is being pursued in MAGICO.

The display of the area-average volume fraction distributions can be understood with the help of Fig. 31; i.e. the averaging is done over horizontal planes through the mixing zone, and are shown as functions of the vertical position and time. The edge of a mixing zone is taken where the fuel volume fraction is 1%.

The results for the fuel volume fractions and of the void fractions are collected along with the melt length scales in Part 2 of Appendix B of DOE/ID-10541. Representative results for two C1 runs at two resolution levels are shown in Fig. 32. It is very interesting to note in these plots how the void fractions build quickly as penetration progresses, how the rate of build-up accelerates with faster break-up, and how the trend of decreasing with time of both the fuel volume fraction and length scales 'doubles-over' (i.e. begin to increase) at some point in time. The length scales increase, at this point in time, because the premixture is essentially voided, and the break-up law used is operative only for as long as the coolant has a void fraction of less than 50%. In regions where this value is exceeded, the break-up process is

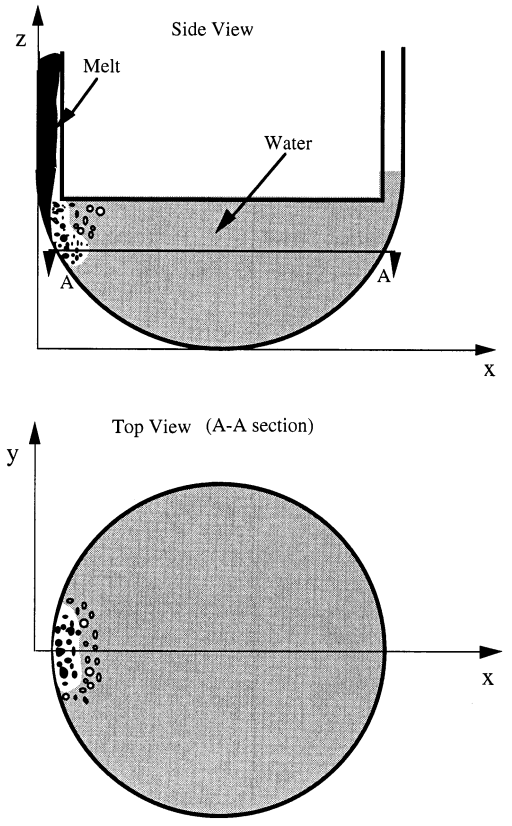

Fig. 31. Illustration of a horizontal plane cut through the premixture, used to compute the area-average volume fractions at the particular elevation.

discontinued. The fuel volume fractions increase, at later times, because of increasing interaction with the counter-current flow coolant vented out from the premixture zone, but a decrease is also observed, it being related to lateral spreading. From the superposition of the fuel volume fraction and void fraction distributions one can obtain a quantitative feel about the location and extent of the non-depleted, potentially explosive, premixtures. These are found at the leading edge, and then decrease with time and with extent of break-up.

The volume-integral results are depicted in Part 3 of Appendix B of DOE/ID-10541. Representative results are shown in Fig. 33. The fuel masses were obtained by integration over all premixture subregions below the initial water level with void fractions less than a given value—five lines are given, the lower most corresponding to 20% void fraction, the topmost one to 100%, and the intermediate ones are in intervals of 20%. Note that the 100% lines should encompass all of the fuel injected, as in fact they do. The important result in these figures is that only a very small fraction of the coolant is found to co-exist with water, the major portion of it being in a highly voided region ($\alpha > 80\%$). Moreover, these figures show that the gradient is very steep, and that the behavior is very similar, independent of break-up behavior, melt injection rates, time, and level of resolution in the calculations. The maximum quantity of melt mixed reaches a maximum of only in the low tens of kilograms; i.e. quantities that from an overall energetic standpoint (i.e. regarding global lower head failure) are not significant.

To appreciate visually the explosive 'quality' of the premixtures, snapshots of the θ_f–α or plane for the two representative cases are presented in Fig. 34. In these maps, the composition of each computational cell is shown as a point, the greyness of which is keyed to a grey length scale. It is clear from these snapshots that the 'sensitive' premixtures are small in size and of a short duration. It is also interesting to note that, at the latter time, the θ_f–α maps converge to a common 'shape', with most points concentrated around the $\theta_f \sim 0$ and $\alpha \sim 90\%$ axis.

Finally, the development of PM-ALPHA.L-3D allows us to assess the effect of numerical diffusion associated with the fully-Eulerian calculations. We consider two cases, the C2-nb and the C2-20.

Typical results (all results can be found in Addendum 2 to Appendix B of DOE/ID10541) are shown in Fig. 35(a,b), comparing the melt and void distribution in pictorial form, and in Fig. 36(a,b), showing the comparisons in the α vs. θ_f plane. In an improved representation relative to that provided in Fig. 34, in these θ_f–α results each cell void fraction is shown as an average value including all contiguously surrounding cells.

Now, in Fig. 35, we observe that the Eulerian melt front early on is surrounded by significantly lower void coolant compared with the Eulerian–Lagrangian results. Moreover, we can see this trend reversing later in time, as the void region

overtakes the 5% fuel contour in the Eulerian result. To this laterally biased melt (and void) distribution contributes a further artificiality of the Eulerian calculation, due to the melt interacting with the horizontal 'steps' of the discretized curved boundary of the domain. This is avoided in the Lagrangian calculation by observing appropriate collision rules for the particle–wall interaction. Quantitatively, these behaviors can be seen in Fig. 36.

What remains yet to be determined is whether local shock loading, with peak amplitudes in the

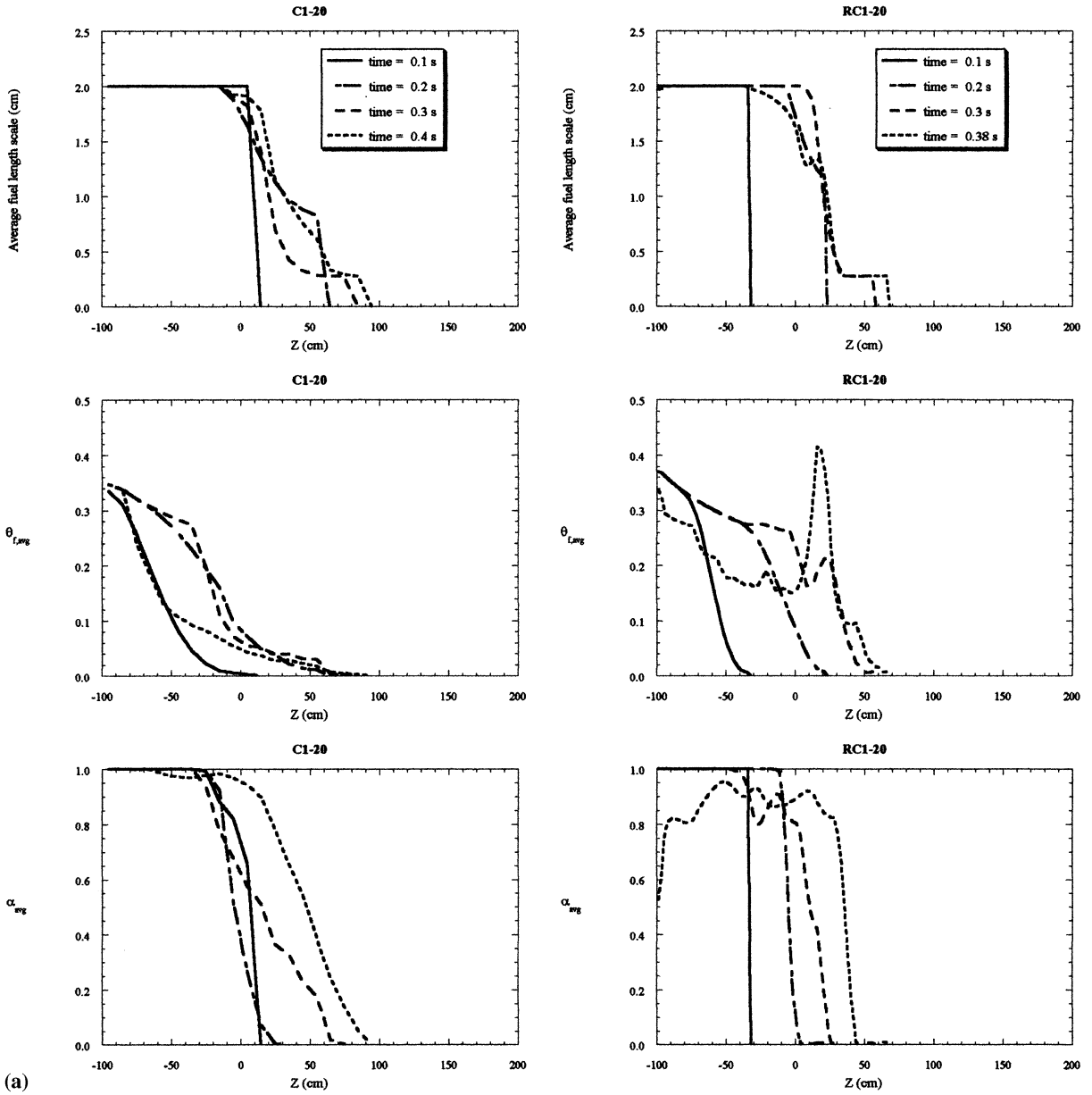

Fig. 32. Axial distribution of area-average quantities (see Fig. 31), and their evolution with time.

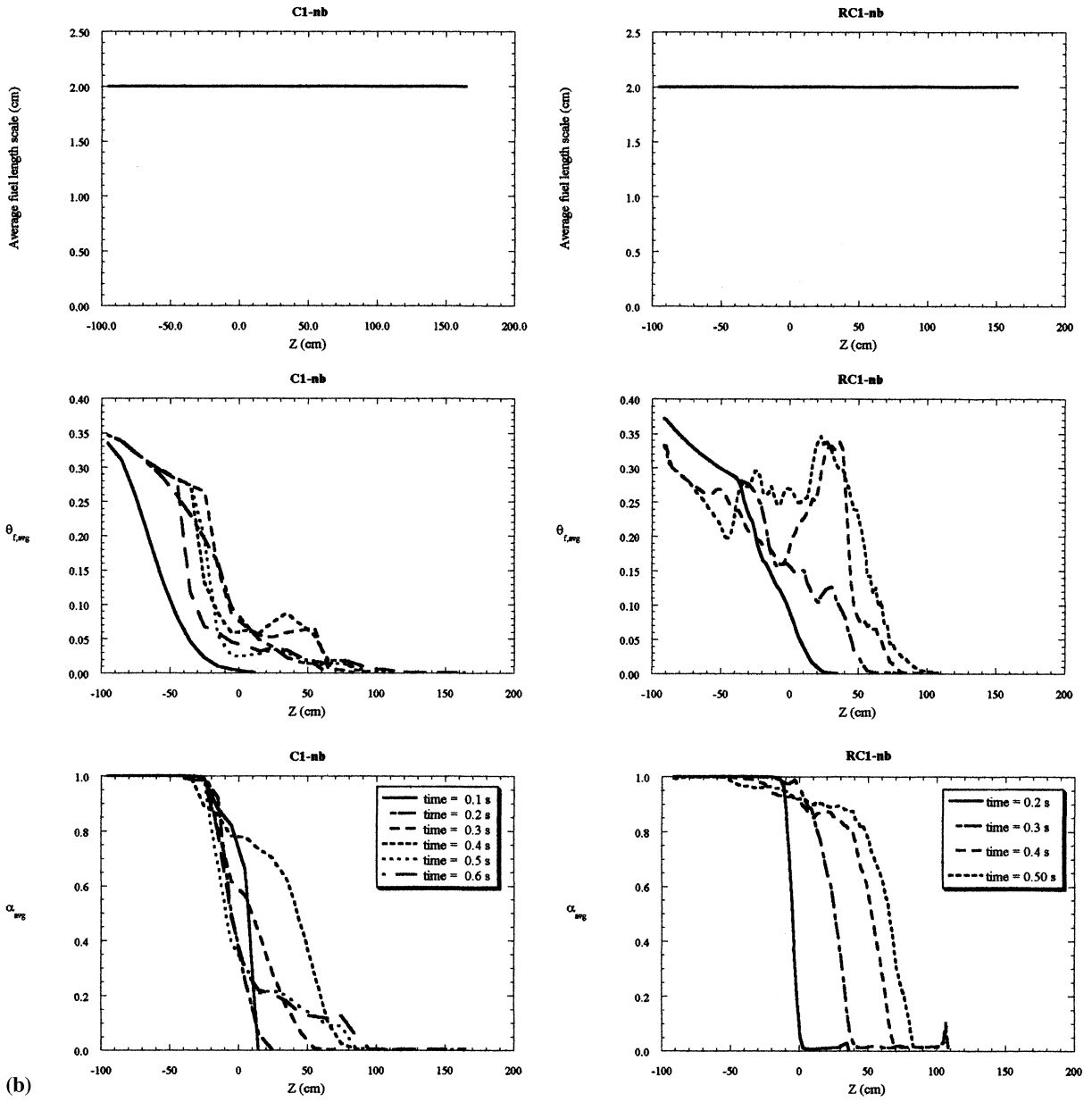

Fig. 32. (*Continued*)

kilobar range, can be of concern for localized damage. Also, what remains to be clarified, regarding such kilobar-level loading, is the interplay between an early trigger, with the fuel mass mixed in the early rise and/or near the maximum, and a late trigger with a lot of fuel in the mixing zone, but most of it surrounded by steam. These are topics taken up in the next section.

The perspectives gained from these results can be enhanced by means of a more focused, mechanistic examination of the melt-stream break-up dynamics. For this purpose, we used the THIR-

MAL code (Chu et al., 1993). For this application, the basic treatment of a cylindrical jet in a free-fall was enhanced to approximately include the presence of two sidewalls (i.e. in the downcomer), as described in Appendix D of DOE/ID-10541. However, the interaction with the curving lower head boundary not being considered, the water depth was set at 0.4 m. These calculations were carried out with equivalent cross-sections corresponding to 5×5 cm^2, 7.5×7.5 cm^2, and 15×15 cm^2 melt release openings, respective pour rates being 14, 39, and 220 kg/s. The results show that the two slower pours break up completely to relatively large particles, 11 mm and 15 mm median sizes, while the large pour yields only 6% break-up, to rather small particles of 2.75 mm median size, which is indicative of a stripping mechanism. The amounts frozen were negligible in all cases. The diameters of the mixing zones, at the top, were about twice the initial jet diameter in all three cases, and the void fractions in them ranged from 40% in the two slow pours, to 75% in the large one. We thus see that both length scales and void fractions are well encompassed by the PM-ALPHA calculations, and that the physics of the situation (melt into saturated water) promote extensive voiding, and discourage extensive, fine scale break-up. Qualitatively, these behaviors are more consistent with the $\beta = 20$ or 'no break-up' cases of PM-ALPHA than the $\beta = 10$ case.

Finally, and for completeness, we may wish to consider also the case of melt being confined to flow very close to the vessel wall, in a film-like fashion. Such flow regimes may arise within the downcomer as the melt 'jumps' the gap at the point of release, spreads somewhat on the wall, and falls as a film. A similar flow regime might exist on the lower head, as the increasing curva-

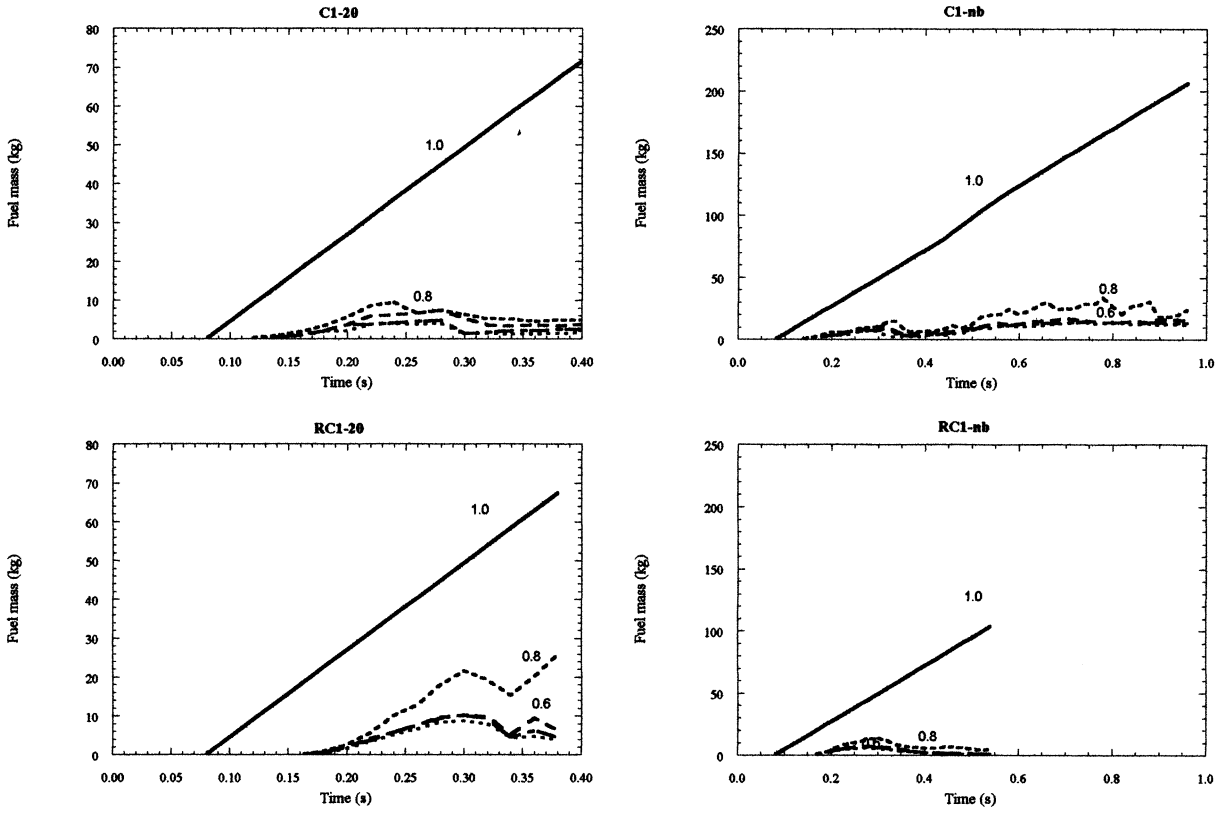

Fig. 33. Fuel mass premixed (see text). The integration (void fraction) intervals are 20, 40, 60, 80, and 100%.

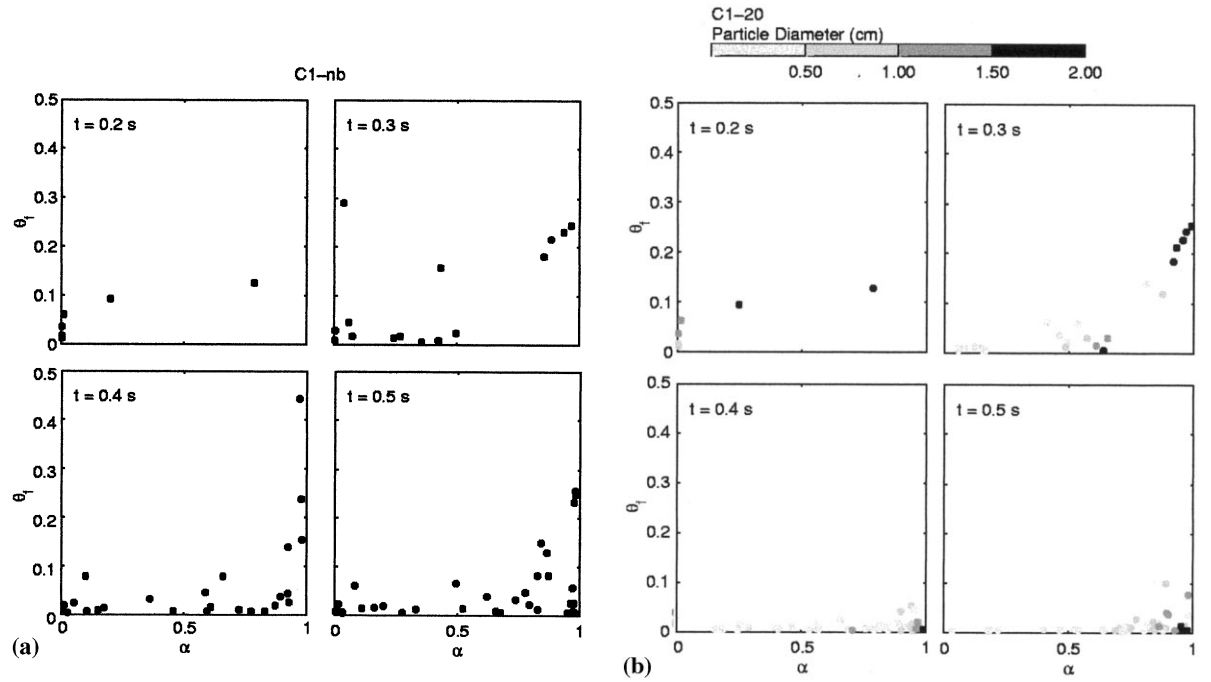

Fig. 34. Snapshots of θ_f–α plane for two representative premixing cases.

ture encountered 'forces' the melt stream against the wall. Such regimes would be like lava flows in hydrovolcanic events, except that saturated water conditions here would produce a highly voided buffer region, effectively preventing contact between melt and water. This would be a benign evolution. Moreover, it is quite clear that such stratified geometries, even if forced to contact, would yield rather benign explosions, due to limited interfacial area for microinteractions.

6. Quantification of explosion loads

As noted already, and as explained in 'The Study', we expect highly voided premixtures, under saturated water conditions to be highly resistant to triggering. Also we expect that this resistance will increase with time as premixture voiding increases too. Moreover, and again as demonstrated in 'The Study', even if triggered, voided premixtures have a highly dampening effect on the resulting explosion energetics. Thus, in bounding the effect of trigger timing on the premixtures of Section 5, we need to look at early rather than later times. This is consistent also from the perspective that a trigger, as normally associated with the melt impacting a wall, should occur when the melt stream is first confronted with a 'turn' at the outer end of the lower head. As illustrated in Fig. 35, this occurs after only about 0.3 s (measured from the times when the fuel is at 1 m above the initial water level).

The calculations were carried out with ESPROSE.m-3D, which is an extension to three dimensions of the original 2D ESPROSE.m code. This new tool, which involves also improved numerics, has been verified by comparison on 1D and axisymmetric problems (run in 3D) with ESPROSE.m. The ESPROSE.m code, on the other hand, has been verified extensively by comparison with experiments and analytical solutions as documented in a special verification report (Theofanous and Yuen, 1998a)

Briefly, our verification approach is based on a 'fitness-for-purpose' attitude, the key features of

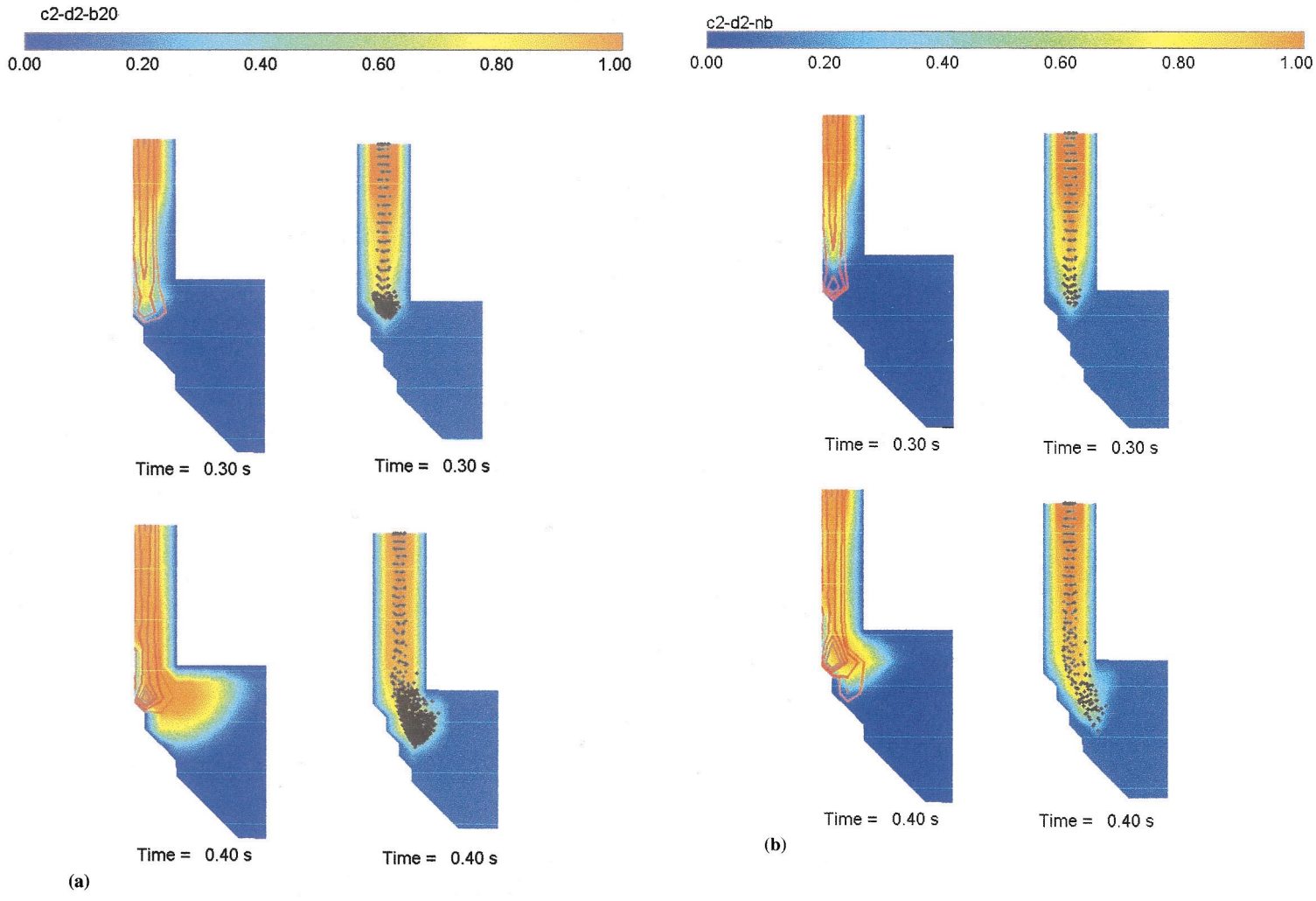

Fig. 35. (a) Pictorial representation of mixing the Eulerian (left column) and Lagrangian PMALPHA calculations. The fuel contours are shown for fuel fractions of 0.05, 0.1, 0.2, 0.3 and 0.4. The case is C2-20. (b) Pictorial representation of mixing the Eulerian (left column) and Lagrangian PMALPHA calculations. The fuel contours are shown for fuel fractions of 0.05, 0.1, 0.2, 0.3 and 0.4. The case is C2-nb.

which are wave dynamics in multiphase media and across phase interfaces, and constitutive laws for the 'microinteractions'. The constitutive laws were obtained, and are currently being further

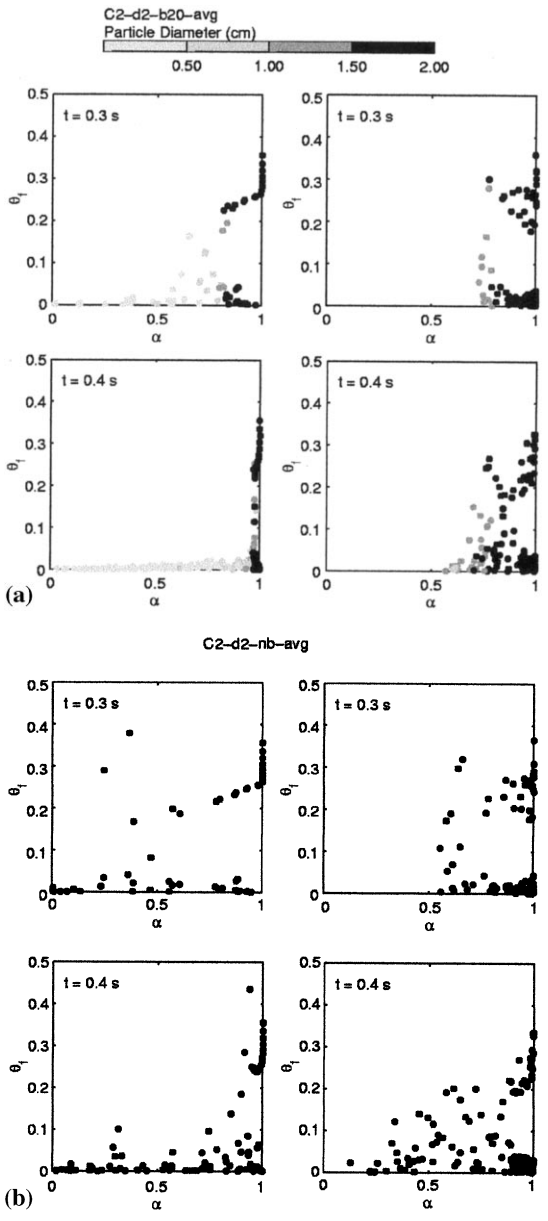

Fig. 36. (a) Quantitative premixing results from the Eulerian (left column) and Lagrangian PM-ALPHA calculations. The case is C2-20. (b) Quantitative premixing results from the Eulerian (left column) and Lagrangian PM-ALPHA calculations. The case is C2-nb.

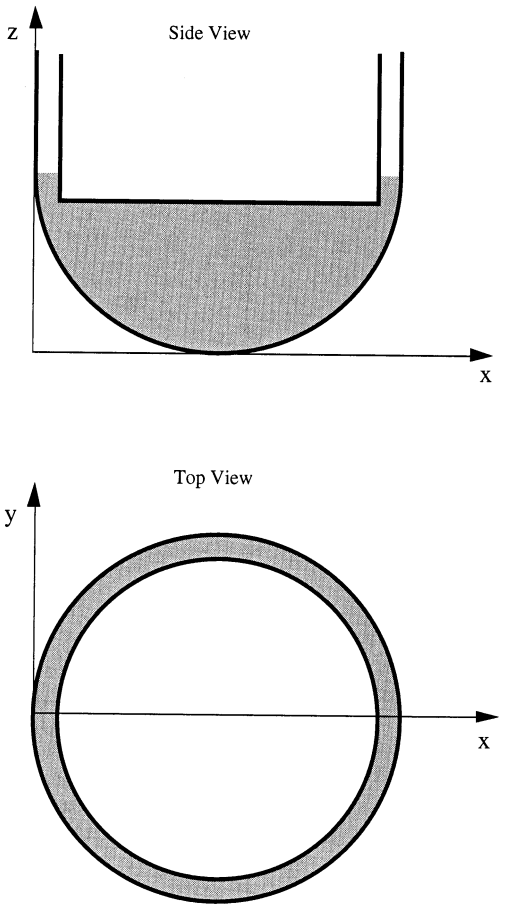

Fig. 37. Coordinate system used in the calculations.

refined, via experiments in the SIGMA facility, and under conditions that simulate large scale, supercritical steam explosions. The wave dynamics were tested by means of analytical solutions, a special purpose code based on characteristics, and by special wave dynamics experiments in SIGMA. The integral behavior was tested against the KROTOS experiments. At this time, we recommend, and use, the values of 7 and 9 for the entrainment factor (f_e) and the fragmentation coefficient (β_f), respectively. The thermal augmentation factor (γ_t) is ramped from a value of 4 at low pressures to a value of 1 at 2000 bar, as discussed in Appendix C of DOE/ID-10503.

The nodalization was the same as in the premixing runs being continued here into explosions.

The coordinate system used is shown in Fig. 37. The runs are denoted by the ID of the corresponding premixture, with the trigger time, in seconds, appended to it in parentheses. That is, ESPROSE.m run C1-10 (0.1) is based on the PM-ALPHA C1-10 premixture, triggered at 0.1 s.

As a trigger, we released steam at 100 bar from one computational cell (or $5 \times 5 \times 5$ cells in the 2 cm grid cases). Numerical tests done previously (Theofanous and Yuen, 1998a) show that the propagation intensity is basically independent of the magnitude of the trigger. However, it is emphasized that our focus here is *not* on triggerability and early escalation, but rather on propagation energetics. Accordingly, our triggers are chosen as sufficient to initiate explosions, and they have no relation to what might arise spontaneously during a pour. Triggerability and early escalation, on the other hand, would require special formulations beyond those afforded in a multifield, continuum frame, and constitutive laws obtained from special SIGMA experiments—such work is planned for some future time.

A total of 31 premixtures were triggered, covering the C1 and C2 cases, and various break-up conditions and trigger times. Three cases with 2 cm grids are triggered to demonstrate the effect of grid size on the predicted load. As in the case of premixing, results are presented in three, successively more integral formats; namely, detailed 3D pressure distributions, local pressure–time histories at selected locations on the lower head (i.e. 'pressure transducer' signals), and impulses at locations of maximum loading. Each set of results is now discussed in turn.

To illustrate the 3D wave dynamics, we chose the two cases found to produce the most intense explosions. Detailed results are summarized in Part 1 of Appendix C of DOE/ID-10541, and a sample is shown in Fig. 38. The explosion primary wave is seen to develop rapidly, and radiate out into the downcomer and lower plenum regions. The decay is seen to be rapid also, due to spatial divergence and venting off the free water surface in the downcomer region. Of principal interest, of course, are the loads shown on the lower head itself. From them, we can obtain a first impression of load intensity (as pressure amplitude and timing) and localization, and hence a basis for first comparisons with the 'screening fragility', in Section 3. These 3D results also provide a good indication of how an explosive event ends up with the pressure completely vented, and the pool at various degrees of upward motion into the downcomer and cold legs.

A more quantitative understanding of the loading, and of explosion dynamics, can be obtained from the 'pressure transducer' signals. The locations of the transducers are shown in Fig. 39, and the results from all runs are summarized in Part 4 of Appendix C of DOE/ID-10541. Sample results are provided in Fig. 40. As the purpose here was to identify the most 'energetic' premixtures, the calculations were carried out to different degrees of completion, depending on how 'interesting' they were found to be. Each explosion run can be related to its own starting premixture, by noting the trigger time and referring to the premixing time of the respective PM-ALPHA run in Appendix B of DOE/ID-10541. Careful consideration of these results shows that the premixing status (i.e. quantity of fuel mixed with low-voids coolant, and extent of voiding of the mixture as a whole) strongly impact the severity of the explosion. This trend, however, can be more conveniently revealed by means of examining the impulse results, which are considered next.

The impulses were computed at the locations of maximum loading, and they are presented along with the pressure transients, and rough estimates of the load localization, in Part 4 of Appendix C of DOE/ID-10541. Sample results are shown in Fig. 41. The area to represent the load localization on the lower head was computed by the

Fig. 38. (a). Pressure distribution for explosion CZ-10 at $t = 0.4$ ms after trigger. Pressures are shown on the lower head, and on planes cutting through the reactor vessel, horizontally, at the position marked. (b) Pressure distribution for explosion C2-10(0.25) at $t = 1.8$ ms after trigger. Pressures are shown on the lower head, and on planes cutting through the reactor vessel, horizontally, at the position marked.

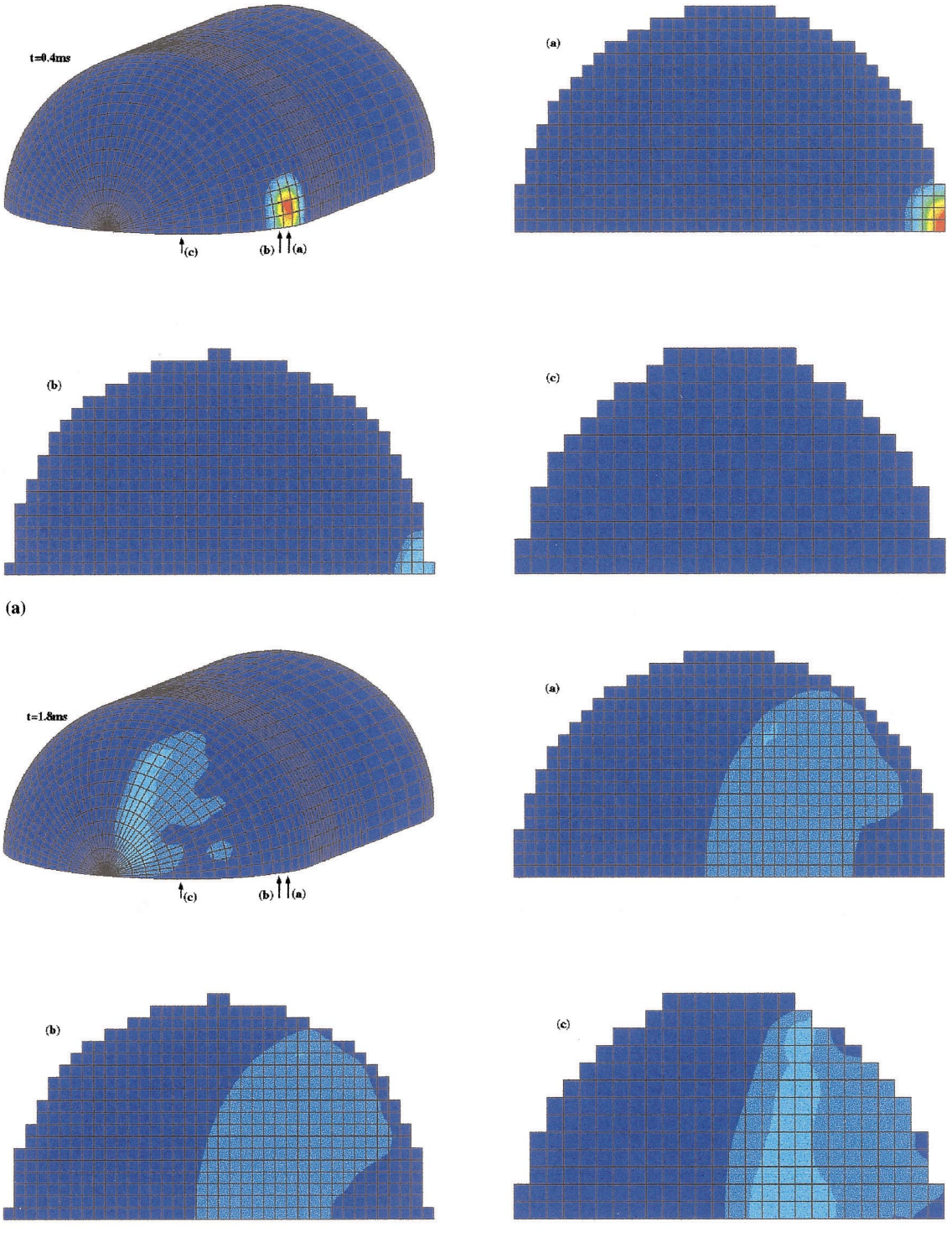

(a)

(b)

Fig. 38.

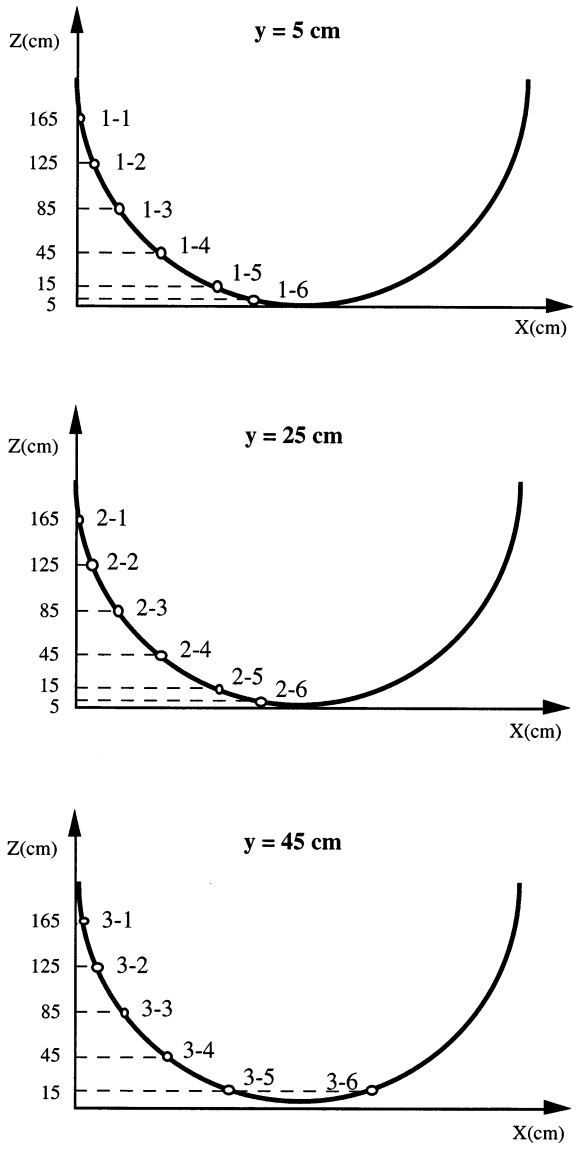

Fig. 39. Identification of 'pressure tranducer' locations on the lower head. The coordinate system used is shown in Fig. 37.

condition that the pressure is within 30% of the pressure at the peak location. The localization factor, d_0/D_s, used in Section 3, can be related to this area, A_0, simply by

$$\frac{d_0}{D_s} \sim 0.5 A_0^{1/2}$$

An overall view of the results is depicted in Table 5, based on which, the following observations can be made.

- Highly broken up premixtures peak in severity very early; intermediate break-up premixtures peak somewhat later; and slightly broken up premixtures remain very benign.
- Peak explosion severity seems to coincide with the peaks observed in quantity of fuel mixed with low to medium void fraction coolant (see Fig. 5.5 and Part 3 of Appendix B of DOE/ID-10541).
- Peak impulses do not depend strongly on the size of the mixing zone (C1 vs. C2 runs).

These observations quantitatively explain the compensating effects of melt length scale and premixture void fraction, as already explained qualitatively on several occasions.

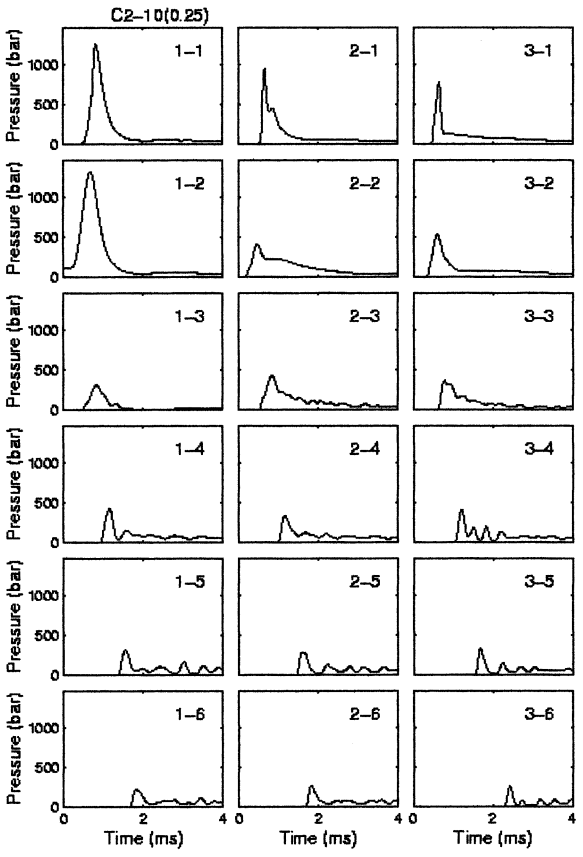

Fig. 40. 'Pressure transducer' signals for run C2-10(0.25). The locations are identified in Fig. 39.

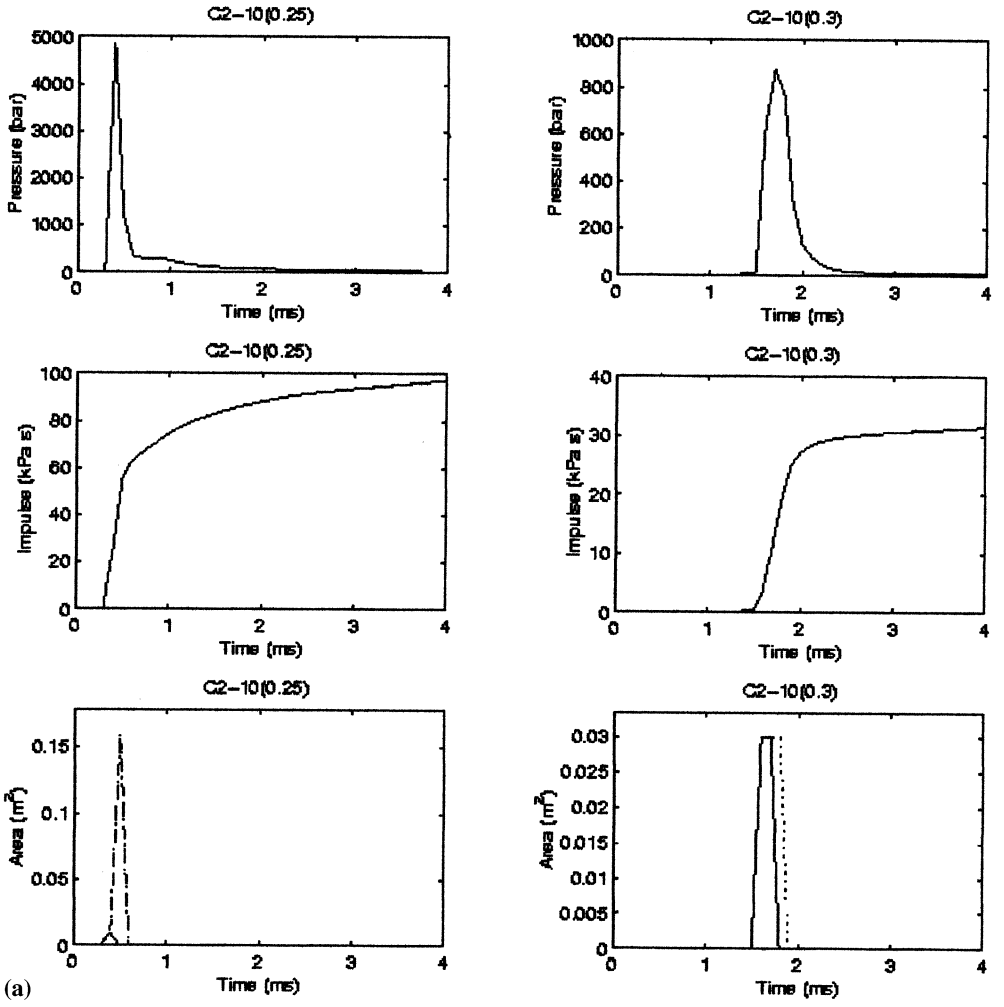

Fig. 41. (a) Pressure, impulse, and effective area (see text) at the location of peak loading. (b) Pressure, impulse, and effective area (see text) at the location of peak loading.

Moreover, these results can be readily used to assess the structural challenge to the lower head by making use of the 'screening fragility' (Fig. 12). For example, we find peak impulses in the 0.1–0.2 MPa s range, and looking up the effective areas and respective effective diameter ratios (d_0/D_s), we find (see Part 3 of Appendix C of DOE/ID-10541) them to be ~ 0.1 m^2 and ~ 0.15, respectively. From Fig. 12, then, we determine that the peak equivalent plastic strain under this load would be essentially zero. This is because, due to the high localization, essentially all energy was redistributed, within the elastic domain, even though a uniform load of such magnitude could produce strains of up to $\sim 10\%$ (see Fig. 7). Thus, none of these explosions could actually pose a significant challenge.

7. Integration and assessment

Normally, in this section, we would be carrying out the operations indicated by the probabilistic framework, but due to the bounding approach we took in regards to CR1 (break-up in premixing) and CR2 (trigger times), this work in a sense has

already been done. Moreover, as shown at the end of Section 6, even the final step, of convoluting the loads to fragility, is not needed here, because they practically do not intersect.

Specifically, what we have found is that even the 10^{-3} premixture (C2, bounded with regard to break-up and trigger timing), would *not* touch the 10^{-3} level of the fragility. Clearly, therefore, the probability of failure is well below 10^{-3}, and such failure, therefore, is physically unreasonable.

This conclusion was further confirmed by using the actual, complete, 3D transient loading, from the two most energetic explosions, directly in the ABAQUS finite shell model of the reactor vessel. The results, that is the final equivalent plastic strains, are shown in Figs. 42 and 43. In these figures, we see that the lower head has hardly entered yielding.

Also in this section, we would normally present a series of arbitrary parametric and sensitivity calculations, to illustrate, for cases where the base results happen to be benign, the margins to failure. This, in effect, has also already been done by the break-up and triggering calculations, in the course of bounding the behavior.

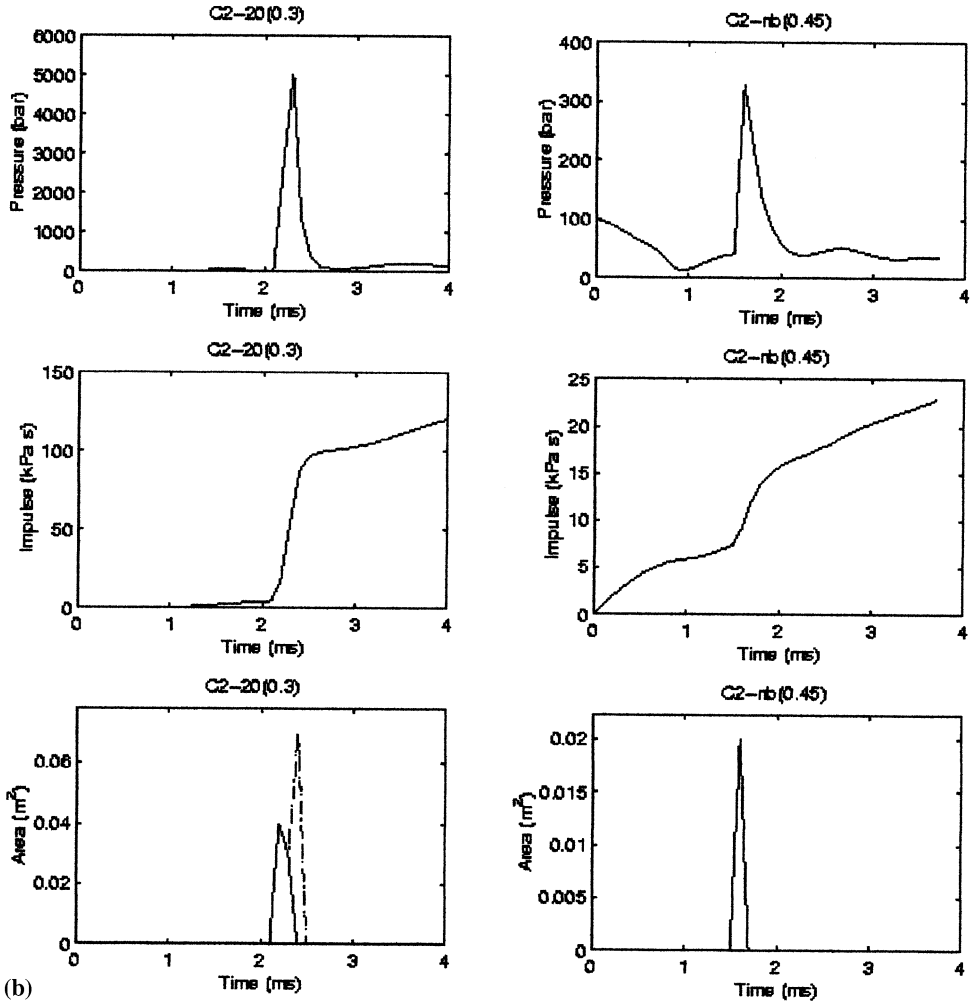

Fig. 41. (*Continued*)

Table 5
Summary of the ESPROSE.m-3D explosion runs[a]

β	C1	RC1	C2	RC2
10	50 (0.23)		100 (0.25)	
	50 (0.24)			
	17 (0.25)			
			90 (0.25)[b]	
			80 (0.25)[c]	
	14 (0.30)		32 (0.30)	
	14 (0.35)		13 (0.35)	
20			100 (0.25)	
	100 (0.30)	110 (0.30)	120 (0.30)	140 (0.30)
	11 (0.35)		14 (0.35)	
	11 (0.40)			
30			100 (0.25)	
			150 (0.30)	
40			90 (0.25)	
			110 (0.30)	
nb	30 (0.25)	17 (0.35)	40 (0.25)	
	45 (0.35)		52 (0.35)	
	17 (0.45)		25 (0.45)	
	26 (1.40)		20 (1.40)	

[a] The entries show the peak local impulse (kPa·s) and the value in parentheses is the trigger time, measured relative to the time ($t = 0$) when the melt is at 1 m above the initial water level. C1 and C2 denote the 200 and 400 kg/s cases, respectively. The nb case denotes 'no break-up'.

[b] Calculation carried out with entrainment factor twice the conservative value normally used.

[c] Calculation carried out with entrainment factor four times the conservative value normally used.

From a more global perspective, we believe that the only way to potentially produce a significant structural challenge on the lower head would be by having a highly subcooled pool in it. Only this would allow sufficient penetration depth, without excessive voids, and as a consequence, both high

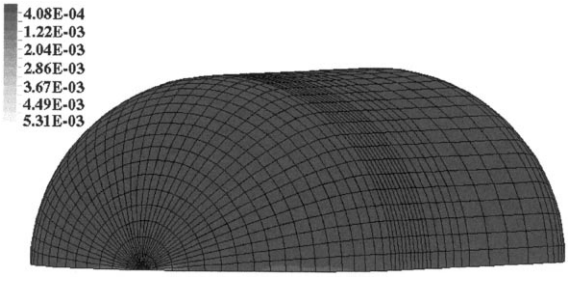

Fig. 42. Final equivalent plastic strain distributions under loading of explosion Run C2-10 (0.25).

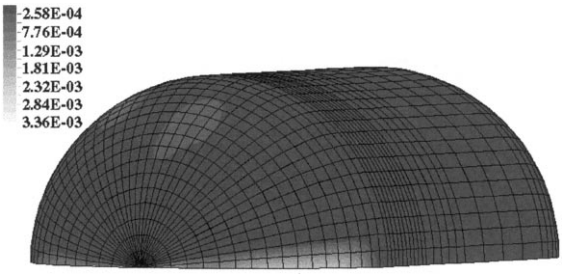

Fig. 43. Final equivalent plastic strain distributions under loading of explosion Run C2-20(0.30).

pressure amplitudes and longer unloading times. This condition, however, cannot be found in AP600 core melt scenarios because, as discussed in Section 4.4, reflooding the vessel would prevent core barrel failure and melt relocation to the lower plenum, altogether.

There may be, of course, a singularity in time, for 'medium' reflood scenarios only (see Fig. 29), in which relocation would begin after initiation of reflood, and just before the added coolant reached the failure location. But even such a scenario would be difficult to yield a highly subcooled condition. The basic reason is that by the time a sufficient amount of water has entered, the total level would have to be well inside the downcomer region, where it would be quickly brought to saturation, and boiling, while being heated from both sides. Moreover, the medium reflood scenario (as is the slow one) arises due to the water level in the containment reaching the break, and since this level rises very slowly, the resulting reflood rate also would be very slow. On the other hand, it is worth noting that even a postulated rapid reflood scenario could not produce the condition of concern, because, for such to occur there would have to be a virtual coincidence, on a time scale of a few tens of seconds, with core barrel failure.

8. Consideration of reflood FCIs

In the IVR Report, we had indicated that a comprehensive consideration of FCIs should include also, besides the premixed explosion regimes

addressed in the rest of the present paper, stratified configurations, as they might arise in late reflood scenarios. By comparison with premixed explosions, stratified interactions are rather benign, and they would not be of concern if it were not for the weakened state of the lower head due to melt attack (see IVR Report). It is the purpose of this section to address this concern.

The geometry, as illustrated in Fig. 44, involves a water stream entering from one of the hot or cold legs, or the direct vessel injection line, and a water layer accumulating on top of the melt. The water enters with a subcooling of ~ 75 K. This high subcooling and relatively high momentum at the point of contact with the melt (~ 3 m fall height) would favor a series of instant small size interactions, rather than delayed 'explosions' involving an accumulated quantity of water. Such small size interactions could have no energetic consequences on the lower head directly, nor could the steam generated have a significant impact on raising the static pressure level (there is ample area for relief through the vent values). To complement this basis of the argument, we will also show that even if a water layer, and a consequent stratified explosion, were to be postulated, it also would be of negligible energetic consequence on the lower head. For this purpose, we will demonstrate that a molten upper surface of the metallic layer (which is a necessary conditions for a propagating, or coherent event) cannot coexist with a quantity of water (on the top) more than some 10 cm in height. Briefly, the reason for this is that the flood rate in the vessel builds up from zero, at a rate controlled by the rate of flood level on the containment floor, while the presence of water on top of the melt leads rapidly to the formation of a solidification front. The consequence of the limited water layer height, on the other hand, is that any potential pressure generated at the interface will vent quickly, thus limiting the magnitude of the impulse generated, down to levels negligible in comparison with the structural capacity of the thinned-out portion of the vessel wall. Details on each one of these topics are provided.

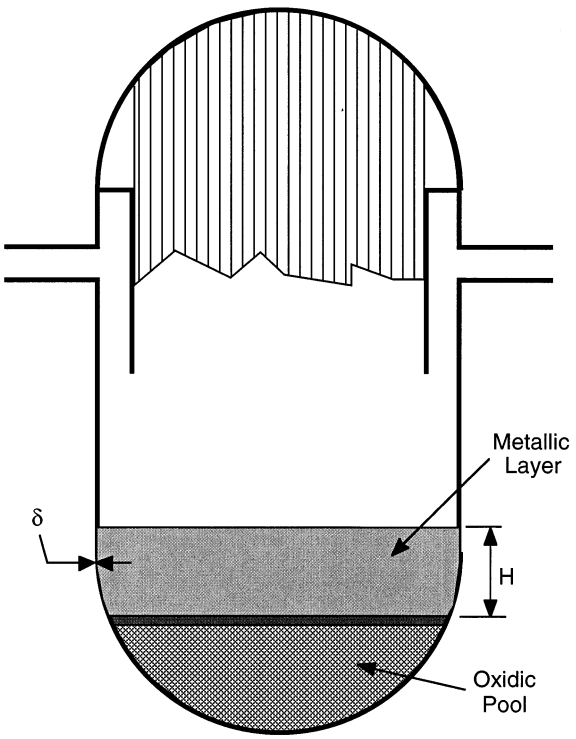

Fig. 44. Illustration of the geometry for a late reflood scenario.

Beginning with the final item, and employing the approach to structural integrity as in Section 3, we find that the impulse generated at the coolant melt interface can be related to the straining of the thinned portion of the vessel wall (see Fig. 44) by

$$I = \sqrt{32\rho\varepsilon\sigma_y}\frac{\delta H}{D} \tag{27}$$

From the IVR Report, $\delta \sim 5$ cm, $H \sim 1$ m, $D = 4$ m, and the average yield stress over the thickness is ~ 160 MPa (still using the conservative value, as in Section 3). For a 20% strain (over the 1 m length), according to Eq. (27), we need an impulse of 35 kPa s.

The potential reflood rates can be derived from the consideration of the three kinds of reflood scenarios found in Section 4.4, and the core melt progression status, discussed in the IVR Report (Appendix 0.3). Therein, we found that the leading intermediate state (LIS) and the final bounding state (FBS), would succeed the first relocation by ~ 30 min intervals. The first relocation was taken to occur about 60 min following the rapid

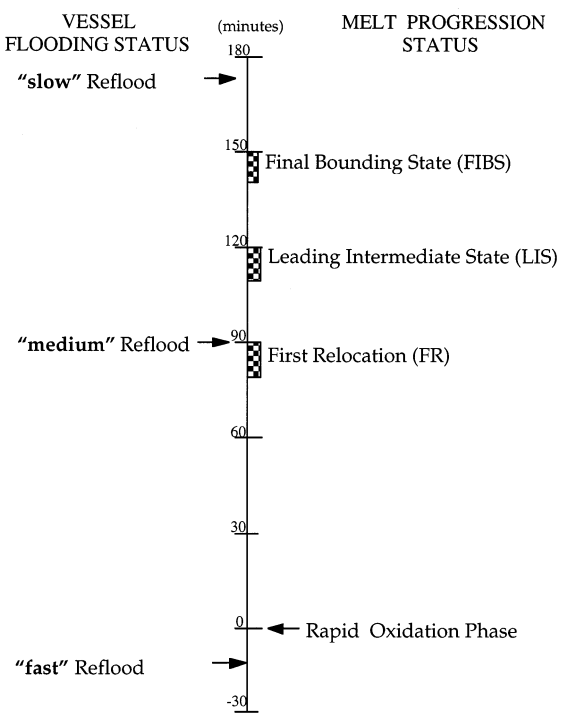

Fig. 45. Definition of potential reflood scenarios from an FCI standpoint.

oxidation phase, which, conservatively for IVR, was bounded by assuming 100% oxidation. For our present purposes, it is more appropriate to use the results of Section 4, and we thus derive the relationship between vessel reflooding and melt progression status as illustrated in Fig. 45. Referring this information to Section 4.4, we can readily conclude that here we need only be concerned about the 'slow' reflood scenario. This is gravity flooding, through one 6-inch line from the in-containment refueling water storage tank (IRWST), that leads to a water-flood rise level, *on the containment floor*, (at the ~ 100 foot elevation), of ~ 0.7 inch/min. Vessel reflooding will occur, as this level covers a break (in the primary system), again as a gravity drain phenomenon, driven by the level-to-break elevation, h. The velocity, at the break, can then be obtained from

$$v \sim \sqrt{hg} \sim \sqrt{agt} \tag{28}$$

where a is the containment flood rate quoted ($\sim 3{\cdot}10^{-4}$ m/s). The water level rise inside the reactor vessel can then be obtained by

$$\bar{U} = \frac{2}{3}\frac{A_e}{A_v}\bar{v} \tag{29}$$

where A_e is the effective area of the break, A_v is the cross-sectional area of the vessel (12.5 m^2), and $\bar{v}$ is the time-average velocity over the vessel flooding period. Thus, for a very small break, such as the one in the direct vessel injection line (10 cm in diameter), over a period of 60 s, we obtain a water accumulation of ~ 1 cm. For a very large break, on the other hand, the effective area will be limited by the submergence itself. For example, for a 0.7 m in diameter break, the effective area after 60 s will be even smaller than that just considered. In the perspective of these numbers, we need to examine next the time needed for initiating a solidification front in the melt, and the pressure levels needed to generate impulses in the range of concern.

The time required for *stable* freezing to begin can be estimated simply by comparing the convection heat flux to the surface from the melt below, to the sum of radiative and film boiling heat fluxes to the coolant above. Taking the surface at the eutectic temperature of 1608 K (see IVR Report), we find that the convective flux is 0.58 MW/m^2, and the radiative flux (an emissivity of 1 is used now) is 0.39 MW/m^2. The difference, 0.19 MW/m^2, can be removed, with a large margin, by film boiling. (Any excess amount of cooling going directly to the latent heat of fusion would determine the rate of crust build-up.) For example, film boiling alone in saturated water (Berenson's correlation) would allow a heat flux of 0.14 MW/m^2, and even a small amount of subcooling could make this number double or triple (Liu and Theofanous, 1995). Thus, freezing should occur virtually simultaneous with the first formation of a subcooled liquid layer.

Taken together, the latter two paragraphs show that only very thin water layers (say below 10 cm) are consistent with a molten metal–coolant interface. However, such thin layers cannot provide sufficient inertial constraint to support propagation, and even if one was to be postulated, both pressures and transient times would be too low to cause structural damage to the lower head. More specifically, using the acoustic unloading time of a 10 cm thick water layer, which is ~ 0.1 ms, a

pressure of 3 500 bar would be required to produce the 35 kPa s impulse found from Eq. (27). Clearly, such an explosive phenomenon, in the geometry of interest here, is not physically possible.

9. Conclusions

The major conclusion of this study is that steam-explosion-induced lower head failure in an AP600-like reactor is 'physically unreasonable.' This, together with a similar conclusion reached on thermally induced failures for an externally flooded AP600 reactor vessel, verifies the validity and robustness of in-vessel retention as a severe accident management strategy.

The principal physical aspects responsible for this favorable conclusion are as follows.

- The saturated coolant condition in the lower plenum, under all relevant scenarios of core melt relocation from the core region. This leads to highly voided premixtures that are hard or impossible to trigger (this is not quantified) and, if a trigger is assumed, to highly damped pressures.
- The 3D, highly transient, nature of the steam explosion loads under such conditions, and the great capacity of the AP600 lower head to withstand such loads (as compared with static and/or uniform loading).
- The melt retentive capacity of the reflector and core barrel, so that even vessel reflood scenarios do not violate the saturation condition noted. In fact, such scenarios would prevent relocation to the lower plenum, and any possibility for steam explosions, altogether. Moreover, such scenarios would further widen the margin relative to the validity of the in-vessel retention strategy, by also preventing the thermal insult on the lower head.
- The formation and permanence of blockages at the lower end of the core, precluding any massive downward relocation through the core support plate. Such a relocation may not be particularly serious, yet an assessment would have to be faced with a number of intangibles, such as coherence of multiple release paths and associate mixing and explosion uncertainties.

Because of the wide margins due to these controlling physics, it has been possible to bound uncertainties to a sufficient degree as to render them of negligible impact on the presented conclusion.

Methodologically (Theofanous, 1996; Theofanous and Yuen, 1998a,b), the assessment involved only a slight scenario dependence, principally on the permanence of the blockages preventing direct downward, through the lower core support plate, relocation. Thus, the assessment is of Grade B, in the ROAAM scale; i.e. involving a single but complex physical process, a slight scenario dependence, being fully supported by scaled experiments, and minimal intangibles treated in a reasonably bounding manner. This work was reviewed by an international panel of 15 experts, as well as by the NRC staff, as documented in Volume 2 of DOE/ID10541. At this time, the phase of development of this problem will reach the maturation status (Phase IV), which is appropriate for use in licensing activities. Phase IV would be expected to receive further contributions from the other advanced reactor designs currently underway (the EPP, for example), as well as from the other efforts worldwide in this currently rather active field of steam explosions.

Future efforts will focus on addressing constitutive laws for break-up during premixing, refining the constitutive laws for microinteractions, extending them to oxidic reactor materials, and expanding the analytical frame and experimental database, to encompass triggering and escalation. In the AP600 context, these are viewed as confirmatory activities, but such progress would be welcome to other applications as well, including larger advanced reactor designs and current reactors.

Acknowledgements

This work is the culmination of many years of effort, by many people, under the sponsorship of two agencies, the US Nuclear Regulatory Commission and the US Department of Energy (under

the Office of Nuclear Energy's ARSAP program). The authors are grateful to past students and colleagues for their contributions along the way, and to the sponsors, whose financial support made it all possible.

For the lead author, it is a special pleasure to acknowledge the encouragement and support obtained all along the way from Dr T.P. Speis (past Deputy Director RES, USNRC), W. Pasedag (USDOE), Steven Sorrell (ARSAP Program Manager, DOE Idaho Operations Office), Dr F. Eltawila (USNRC) and Stephen Additon (TENERA).

We would also like to take this opportunity to express our appreciation and thanks to Dr L. Baker and Dr L.W. Deitrich for their cooperation in managing this effort for Argonne National Laboratory, and to the Experts who participated as reviewers (see Appendix E of DOE/ID-10541).

Appendix A. Nomenclature

A	area
C	wall coefficient
$\hat{c}$	heat capacity
d	diameter
D	diameter, or material parameter in Eq. (1)
e	internal energy
f_r	radiation factor in Eq. (13)
g	acceleration gravity
h	heat transfer coefficient
I	impulse
k	thermal conductivity
L	length
$\dot{m}$	mass addition rate
Nu	Nusselt number $= hL/k$
p	material parameter in Eq. (1), or rod pitch
q	heat flux
$\dot{Q}$	decay power density
Ra′	Rayleigh number $= \beta\dot{Q}L^5/v\alpha k$
T	temperature
t	time
R	radius
Greek letters	
α	thermal diffusivity, or void fraction
β	break-up parameter value, or thermal expansion coefficient
δ	wall thickness
ϵ	plastic equivalent strain, or emissivity
$\dot{\varepsilon}$	strain rate
θ	volume fraction
λ	crust growth constant
ρ	density
σ	stress, or Boltzmann constant
Subscripts	
b	bending; bulk; bottom; or blockage
c	crust
dn	downward direction
e	effective, or edge
hr	horizontal direction
i	inner
l	metal layer
m	melt
max	maximum value
o	initial value, or outer value
p	pool
r	radiation
s	sphere, or solid
up	upward direction
w	wall, or water
y	yield
3D	local value
Superscripts	
D	dynamic
+	characteristic value
*	dimensionless value

References

AMIGO Seminar, 1995. Proceedings of US (NSF) Japan (JSPS) Joint Seminar, A Multidisciplinary International Seminar on Intense Multiphase Interactions. Santa Barbara, CA, 9–13 June.

Bodner, S.R., Symonds, J., 1962. Appl. Mech. 29, 719.

Bohl, W.R., Butler T.A., 1985. Some comments on the probability of containment failure from steam explosions, contribution to the Steam Explosion Review Group report, NUREG-1116. US Nuclear Regulatory Commission, February.

Carslaw, H.S., Jaeger, J.C., 1959. Conduction of Heat in Solids, 2nd ed. Oxford University Press, Oxford.

Chu, C.C., Sienicki, J.J., Spencer, B.W., 1993. THIRMAL-1 computer code for analysis of interactions between a stream of molten corium and a water pool, volume 1: code manual TR-103417-V1. Research Project 3130-01, Final Report. Argonne National Laboratory, December.

CSNI, 1993. Proceedings of the CSNI Specialists Meeting on Fuel-Coolant Interactions. Santa Barbara, CA, 5–8 January. NUREG/CP-0127, March 1994.

Duffey, J., Mitcheli, D., 1973. Containment of explosions in cylindrical shells. Int. J. Mech. Sci. 15, 237–249.

Fletcher, D.F., Theofanous, T.G., 1997. Heat transfer and fluid dynamic aspects of explosive melt-water interactions. Adv. Heat Transfer 29, 129–213.

Hohmann, H., Magallon, D., Schins, H., Yerkess, A., 1995. FCI experiments in the aluminum oxide/water system. Nucl. Eng. Design 155, 391–403.

Huhtiniemi, I., Hohmann, H., Magallon, D., 1995. FCI experiments in the corium/water system. Proceedings of the 7th International Meeting on Nuclear Reactor Thermal Hydraulics NURETH-7. Saratoga Springs, NY, 10–15 September, NUREG/CP0142, pp. 1712–1727.

Johnson, G.R., Cook, W.H., 1985. Fracture characteristics of three metals subjected to various strains, strain rates, temperatures and pressures. Eng. Fracture Mech. 21, 31–48.

Korhonen, A.S., 1987. On the theories of sheet metal necking and forming limits. J. Eng. Mater. Technol. 100, 303.

Kymäläinen, O., Tuomisto, H., Hongisto, O., Theofanous, T.G., 1993. Heat flux distribution from a volumetrically heated pool with high Rayleigh number. Proceedings NURETH-6. Grenoble, 5–8 October [see also 1994, Nucl. Eng. Design 149, 401–408].

Liu, C. Theofanous, T.G., 1995. Film boiling on spheres in single- and two-phase flows. Part I: experimental studies. ANS Proceedings, 1995 National Heat Transfer Conference. Portland, OR, 5–9 August, pp. 34–37.

Manteufel, R.D., 1991. Heat transfer in an enclosed road array. Ph.D. Thesis, Massachusetts Institute of Technology.

Manteufel, R.D., Todreas, N.E., 1994. Effective thermal conductivity and edge conductance model for a spent-fuel assembly. Nucl. Technol. 105, 421.

Nourgaliev, R.R., Dinh, T.N., Sehgal, B.R., 1997. Effect of fluid Prandtl number on heat transfer characteristics in internally heated liquid pools with Rayleigh numbers up to 10^{12}. Nucl. Eng. Design 169, 165–184.

OJI, 1993. Proceedings of the International Seminar on The Physics of Vapor Explosions. Tomakomai, Hokkaido, Japan, 25–29 October.

Okkonen, T., Wennerström, H., Hedberg, S. Blomstrand, J. Sehgal, B.R. Frid, W., 1996. Film boiling on a long vertical surface under high heat flux and water subcooling conditions. Proceedingsof the 1996 National Heat Transfer Conference. Houston, TX, 3–6 August.

Olive, F., Nicaud, A. Marilleau J. Loichot, R., 1979. Rupture behavior of metals in explosive expansion. Institute of Physics Conference Series, No. 47. The Institute of Physics Publishing, Ltd., Bristol, UK, pp. 242–251.

Pao, Y.H., Gilat, A., 1992. High strain rate deformation and failure of A533B steel at various temperatures. Acta Metall. Mater. 40, 1271–1280.

Scobel, J.H., Theofanous, T.G., Sorrell, S.W., 1996. Application of the risk oriented accident analysis methodology (ROAAM) to severe accident management in the AP600 advanced light water reactor. Proceedings of the PSA '96 International Topic Meeting on Probabilistic Safety Assessment, Park City, UT, 29 September–3 October, vol. II, 915–923

SERG2, 1995. A reassessment of the potential for an alpha-mode containment failure and a review of the current understanding of broader fuel-coolant interaction (FCI) issues. Report of the Second Steam Explosion Review Group Workshop, NUREG1529. US Nuclear Regulatory Commission, Washington, DC.

Shockey, D.A., Seaman, L., Dao, K.C., Curran, D.R., 1980. Kinetics of void development in fracturing A533B tensile bars. J. Pressure Vessel Technol. 102, 14–21.

Steinberner, U., Reineke, H.-H., 1978. Turbulent buoyancy convection heat transfer with internal heat sources. Proceedings of the Sixth International Heat Transfer Conference. Toronto, Canada, August.

Theofanous, T.G., 1996. On the proper formulation of safety goals and assessment of safety margins for rare and high-consequence hazards. Reliability Eng. Systems Safety 54, 243–257.

Theofanous, T.G., Yuen, W.W., 1994. The prediction of dynamic loads from ex-vessel steam explosions. Proceedings of the International Conference on New Trends in Nuclear System Thermohydraulics. Pisa, 30 May–2 June, pp. 257–270.

Theofanous, T.G., Yuen, W.W., 1998a. Escalation and propagation of steam explosions: ESPROSE.m verification studies. DOE/ID-10503, June. US Department of Energy.

Theofanous, T.G., Yuen, W.W., 1998a. Premixing of steam explosions: PM-ALPHA verification studies. DOE /ID-10504, June. US Department of Energy.

Theofanous, T.G., Najafi, B., Rumble, E., 1987. An assessment of steam-explosion-induced containment failure. Part I: probabilistic aspects. Nucl. Sci. Eng. 97, 259–281.

Theofanous, T.G., Liu, C., Additon, S., Angelini, S., Kymäläinen, O., Salmassi, T., 1995a. In-vessel coolability and retention of a core melt. DOE/ID-10460, Vols. 1 and 2, July. US Department of Energy.

Theofanous, T.G., Yuen, W.W. Angelini S. Chen, X., 1995b. The study of steam explosions in nuclear systems. DOE/ID-10489, January. US Department of Energy.

Turland, B.D., Fletcher, D.F., Hodges, K.I., Attwood, G.J., 1995. Quantification of the probability of containment failure caused by an in-vessel steam explosion for the Sizewell B PWR. Nucl. Eng. Design 155, 445–458.

Yuen, W.W., Theofanous, T.G., 1995. The prediction of 2D thermal detonations and resulting damage potential. Nucl. Eng. Design 155, 289–309.

Yuen, W.W., Chen, X., Theofanous, T.G., 1994. On the fundamental microinteractions that support the propagation of steam explosions. Nucl. Eng. Design 146, 133–146.